Preliminary orbital analysis for a CubeSat mission to the Didymos binary asteroid system

Elsevier Editorial System(tm) for Advances in Space Research

Manuscript Draft

Manuscript Number: ASR-D-17-00377R2

Title: Preliminary Orbital Analysis for a Cubesat Mission to the Didymos Binary Asteroid System

Article Type: SI: Small Body Exploration

Keywords: Orbital analysis; Navigation; Binary asteroids; Cubesat; Didymos

Corresponding Author: Dr. Riccardo Lasagni Manghi, M.D.

Corresponding Author's Institution: University of Bologna

First Author: Riccardo Lasagni Manghi, M.D.

Order of Authors: Riccardo Lasagni Manghi, M.D.; Dario Modenini; Marco Zannoni; Paolo Tortora

Abstract: Nanosatellite missions represent a promising option for the exploration of the near-Earth asteroid population since they provide low-cost versatile platforms for scientific observations. This paper describes the preliminary orbital and navigation analyses for the DustCube mission, which was pre-selected to reach the binary asteroid system Didymos on-board ESA's AIM spacecraft. Possible candidate orbits that exploit the binary nature of the system are identified and traded off to produce a preliminary concept of operations. The overall feasibility of the proposed scenario is then addressed by integrating the spacecraft trajectories in a realistic dynamical environment, evaluating their sensitivity to state errors, and estimating the accuracy of the orbit determination system.
Preliminary results suggest that autonomous navigation of a Cubesat platform within a binary asteroid system is technically feasible. The proposed solution, which combines an initial parking orbit at the L4 equilibrium point with a Distant Retrograde Orbit for proximity operations, is shown to be consistent with the estimated orbit determination accuracy and allows to fulfil the mission requirements.

Preliminary Orbital Analysis for a Cubesat Mission to the Didymos Binary Asteroid System

Riccardo Lasagni Manghi[*1], Dario Modenini[†], Marco Zannoni[‡], Paolo Tortora[°]

* Ph.D. student, University of Bologna, Department of Industrial Engineering, via Fontanelle 40, 47121, Forlì (FC), Italy.
† Assistant Professor, University of Bologna, Department of Industrial Engineering, via Fontanelle 40, 47121, Forlì (FC), Italy.
‡ Research Assistant, University of Bologna, Department of Industrial Engineering, via Fontanelle 40, 47121, Forlì (FC), Italy.
° Associate Professor, University of Bologna, Department of Industrial Engineering, via Fontanelle 40, 47121, Forlì (FC), Italy.

1 Abstract

Nanosatellite missions represent a promising option for the exploration of the near-Earth asteroid population since they provide low-cost versatile platforms for scientific observations. This paper describes the preliminary orbital and navigation analyses for the DustCube mission, which was pre-selected to reach the binary asteroid system Didymos on-board ESA's AIM spacecraft. Possible candidate orbits that exploit the binary nature of the system are identified and traded off to produce a preliminary concept of operations. The overall feasibility of the proposed scenario is then addressed by integrating the spacecraft trajectories in a realistic dynamical environment, evaluating their sensitivity to state errors, and estimating the accuracy of the orbit determination system.
Preliminary results suggest that autonomous navigation of a Cubesat platform within a binary asteroid system is technically feasible. The proposed solution, which combines an initial parking orbit at the L_4 equilibrium point with a Distant Retrograde Orbit for proximity operations, is shown to be consistent with the estimated orbit determination accuracy and allows to fulfil the mission requirements.

Keywords: Orbital analysis; Navigation; Binary asteroids; Cubesat; Didymos

2 Introduction

In recent years, the number of mission proposals towards small celestial bodies is generally increasing, and consequently a growing interest can be observed for scientific studies on spacecraft dynamics within such environments. A few mission concepts have already been developed that involve binary asteroid systems of small irregular bodies, which are estimated to represent a significant portion of the near-Earth asteroid population. In particular, the Asteroid Impact Deflection Assessment (AIDA), currently under joint development by ESA and NASA, plans to target the binary asteroid system Didymos (Cheng et al., 2015). This scenario aims at demonstrating the kinetic impactor concept, which consists in modifying the asteroid trajectory by impacting the smaller component of the binary system.

The AIM (Asteroid Impact Mission) probe is intended to be watching closely as DART (Double Asteroid Redirection Test) hits the smaller asteroid, informally called Didymoon, at a speed of approximately 6 km/s. In the aftermath, it will perform detailed before and after comparisons on the structure of the body itself and on its orbit in order to characterize DART's kinetic impact and its consequences (Cheng et al., 2016), (Michel et al., 2016).

In addition to its own scientific payload, the original AIM spacecraft concept (now being reshaped to become lighter and more affordable, see Michel et al, 2017) was designed to carry at least three smaller spacecraft: the Mascot-2 asteroid lander, developed by DLR, and two or more CubeSat

[1] Corresponding Author, riccardo.lasagni@unibo.it, +39 0543 374450

Opportunity Payloads Independent Nano-Sensors (COPINS), which will serve to demonstrate deep-space inter-satellite communications for independent CubeSat-based sensors and allow to perform measurements that are deemed too high a risk for the AIM spacecraft. DustCube, a nanosatellite-based mission concept for a 3U CubeSat developed jointly by the University of Vigo (S), the University of Bologna (I), and Micos Engineering GmbH (CH), is one of the five COPINS proposals that were selected by ESA for further study. Its main goal is to enhance the capability of the AIM spacecraft to elucidate the properties of the natural dust environment of the Didymos system and to quantify and characterize the ejecta plume created during DART's impact by using a high definition light-scattering Nephelometer for remote (RNH) and in-situ (INH) measurements (Perez, et al., 2017, submitted)

This paper is organized as follows: Section 3 gives an overview of the preliminary Orbital Analysis and of the Concept of Operations for the described mission; this includes a description of the mission requirements and constraints, an evaluation of the dominant perturbing accelerations acting on the system and a description of the numerical tools and procedures that were used to identify possible candidate orbits. The selected orbits are further evaluated by addressing their behaviour inside a complex dynamical model and by estimating their sensitivity to orbit determination errors. The deployment from AIM mothership is then addressed, along with the station-keeping strategy, the ADCS design and the total ΔV budget.

Section 4 describes the overall navigation approach; this includes a description of DustCube's optical navigation principles and of the general layout of the Orbit Determination and Control System. An estimation of the orbit determination accuracy is given through a numerical simulation, based on a pure geometric approach, together with the estimation of its computational burden.

Finally, Section 5 summarizes the results and identifies further investigations to be performed in the subsequent phases of the mission development.

3 Orbital Analysis and Concept of Operations

3.1 DustCube Mission constraints

The orbital and navigation analyses described in the following sections rely on a series of assumptions and requirements, which were derived from the DustCube scientific objectives and from the latest Concept of Operations (CONOPS) for the AIM and AIDA missions available at the time of the present work:

1) DustCube should navigate at close range from the binary system, and in particular at a maximum distance of 3 km from Didymoon to allow for the use of the Remote Nephelometer (RNH) and In-situ Nephelometer (INH) for the characterization of the dust particles in the Didymos environment.

2) Although ground-based navigation techniques have proven to be suitable for operations around small bodies in deep space, as for Rosetta mission (Godard et al, 2015), the required proximity to the two asteroids and the associated short time-scales for the orbital motion make this solution unpractical during most of DustCube's operational phases. An autonomous optical navigation concept is thus to be preferred, which should rely on AIM's Inter-satellite link (ISL) only as a backup solution.

3) Didymos physical parameters are still highly uncertain and their estimated values may change as new observations of the system become available. Any proposed concept of operations should cope with this uncertainty and either foresee an autonomous estimation of these parameters or allow for periodic updates during the successive characterization phases of the AIM mission.

4) The CONOPS for the AIDA mission foresees a time interval of roughly two months between the Payload Deployment Phase (PDP) and DART's impact on Didymoon. Proposed mission concepts should thus employ stable parking orbits to reduce the amount of station-keeping manoeuvers and propellant consumption to levels which are compatible with COTS orbital and attitude control systems for Cubesats.

5) COPINS deployment is foreseen to occur at a variable altitude from Didymos barycentre, ranging from a close-up PDP altitude of less than 2 km (required for Mascot landing) and an altitude of 10 km, where AIM will return for the rest of the Detailed Characterization Phase (DCP). The release mechanism allows for deployment speeds down to $5\ \mathrm{cm/s}$ with an accuracy of $\pm 1\ \mathrm{cm/s}$ along the

deployment axis. Proposed injection strategies should thus cope with these constraints and mitigate the effect of the injection error.

3.2 Major orbital perturbations

To explore the dynamical behaviour of the Didymos system, a first step may be represented by the estimation of the dominant perturbing effects as a function of the baseline orbit around the Didymos barycentre. Previous investigations examined this problem for both single (Scheeres, 1994) and binary asteroids (Chappaz et al., 2015) by considering the perturbations from solar tide, SRP, oblateness of the primary asteroid and third-body effect. The approach discussed by Scheeres consists in estimating the strength of the perturbations by identifying common coefficients in the Lagrange Planetary Equations that are obtained using the potential perturbing function which is being evaluated. By limiting the analysis to the second order in inclination and eccentricity terms and evaluating only the secular variations of the orbital parameters, the expressions for these strength coefficients simplify to:

$$C_{SRP} = \frac{3gna^2}{2\mu_S} \qquad (1)$$

$$C_{OBL} = \frac{3nJ_2\alpha_0^2}{2\alpha^2}v \qquad (2)$$

$$C_{3BE} = \frac{\mu_2}{4na^3}\alpha\bar{\alpha}b_{3/2}^{(1)} \qquad (3)$$

Where n represents the mean motion of the s/c around the binary system, μ_2 and μ_S represent the gravitational parameters of Didymain and of the overall Didymos system respectively and a is the semi-major axis of the reference orbit. In the expression for the SRP, $g = G_1 B/R^2$ represents the SRP acceleration, G_1 is the solar flux constant and B is the effective area to mass ratio of the s/c. Also, in the expression for the 3rd body effect, $\alpha = {}^{a}/_{a_2}$ where a_2 is the semi-major axis of Didymoon's relative orbit and $b_{3/2}^{(1)}$ is the Laplace coefficient defined as:

$$b_{3/2}^{(1)} = \frac{1}{2}\int_0^{2\pi} \frac{cos\varphi}{(1-2\alpha cos\varphi+\alpha^2)^{3/2}}\,d\varphi \qquad (4)$$

Figure 1 shows the strength of the various perturbing effects as a function the semi-major axis, assuming a baseline circular orbit and considering values of the un-normalized coefficient $J_2 = 1.2 \cdot 10^{-2}$ (Zannoni et al., 2017) and $B = 0.02\ m^2/kg$.

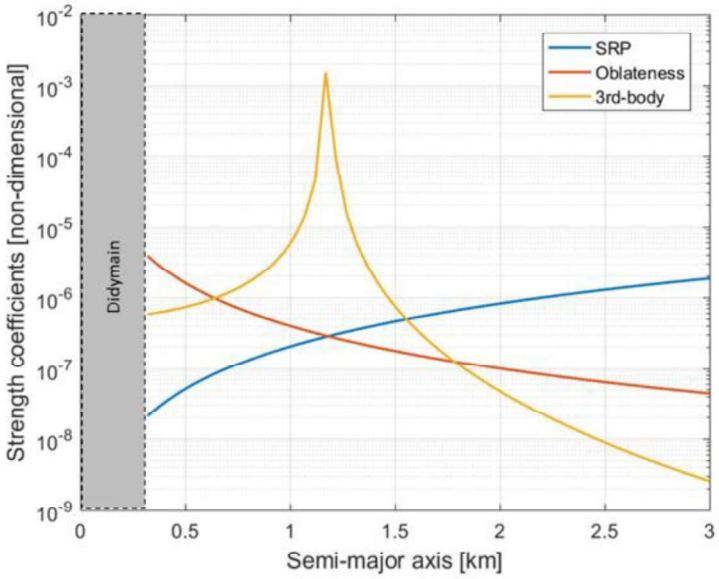

Figure 1 Strength of the perturbing effects vs. orbit semi-major axis. The grey region represents the surface of Didymain.

The zonal map depicted in Figure 1 was also employed to determine which types of orbits were more practical to support the current mission scenario. For instance, trajectories that are driven by SRP, e.g. terminator orbits, are most useful for scenarios where the s/c orbits at a large distance from the primary (Broschart et al., 2014). Conversely, the DustCube scenario requires that the s/c remains mostly in the neighbourhood of Didymoon, where trajectories derived from the Circular Restricted Three-Body Problem (CR3BP) may prove more useful. Due to this reason, priority was given in the present study to the analysis of orbits that are characteristic of the three-body problem and that remain in the vicinity of Didymoon for most of their orbital period.

3.3 Orbital analysis general approach

The subsequent orbital analysis was performed through a series of successive steps:

1) At first, closed periodic orbits were obtained in the simplified CR3BP using a differential correction algorithm that makes use of the State Transition Matrix. By varying the initial s/c state with a continuation method, a wide array of orbital families was found.

2) A dynamic catalogue of candidate orbits was created by computing the values of some characteristic parameters, which vary continuously along the orbital families. These parameters were then used to identify the most suitable orbits to satisfy the mission requirements and constraints.

3) Proposed orbital solutions were traded off to produce a preliminary Concept of Operations (CONOPS). This preliminary concept included different scenarios with an increasing level of risk and a corresponding benefit in the scientific return for the mission.

4) In an initial assessment of the robustness and stability of a given solution, candidate orbits obtained in the CRTBP model were integrated in the so called High Fidelity Ephemerides (HFE) model, described in Section 3.6**,** which should accurately approximate the real dynamical system.

3.4 Candidate orbits and selection methodology

The identification of candidate orbits was performed using the approach described by (Parker & Anderson, 2013). At first, the dynamical equations of a non-dimensional CR3BP were implemented numerically and s/c trajectories were integrated starting from an initial state of the kind $X_0 =$

$(x, 0, z, 0, \dot{y}, 0)^T$, where the coordinates are referred to the synodic reference frame that is co-rotating with the system primaries. A single-shooting differential correction algorithm that makes use of the State Transition Matrix (STM) was then implemented to modify the initial conditions and generate close periodic orbits. Once a single periodic orbit was found, a continuation method was applied to traverse that orbit's family by slightly modifying the initial conditions according to a quadratic prediction scheme, which uses three previous state values along a family to estimate the successive one.

The result of applying this technique to the problem under consideration was the generation of a database of symmetric periodic orbits whose general behaviour is already known from previous studies (Chappaz & Howell, 2014). Several orbital families were explored, among which we highlight: *Planar Lyapunov* orbits in the vicinity of the collinear libration points, *Distant Prograde Orbits* (*DPOs*) about both of the primaries, *Distant Retrograde Orbits* (*DROs*) about the smaller primary and *Halo orbits*, which represent a natural out-of-plane continuation of the Lyapunov orbits.

Following the approach outlined by (Folta et al., 2015), each orbit in this database was characterized through a series of key parameters, which were used to efficiently guide the trajectory design and perform a trade-off between alternative scenarios. These included:

1) *Distance from Didymoon*, which was used to verify the fulfilment of the line-of-sight constraints for the RNH dust observations.

2) *Orbital period*, which gives an indication about the speed of the dynamics and the frequency of station-keeping manoeuvres.

3) The *Jacobi constant*, which gives an estimation of the s/c energy along its orbit and may be used to provide a rough estimation of the minimum cost required to transfer between two separate orbits. In fact, the transfer Δv between two orbits may have an effect on both the magnitude and the direction of the velocity, and must, at minimum, allow for the energy change, i.e. the adjustment of the Jacobi constant value.

4) The *Stability index*, which can be used to gain an immediate insight into the overall stability of the orbit under examination and is defined as the average of each reciprocal pair of eigenvalues of the Monodromy matrix. In particular, if any of the stability indexes associated with the three couples of conjugate eigenvalues is bigger than one, the orbit is unstable.

5) The perturbation *halving time* (or doubling time in case of unstable orbits), which can give an idea of the relative stability between the different orbits by taking into account the different timescales of the orbital motion.

Evaluating the maximum stability indexes for the various orbital families, only the DROs and some of the DPOs showed a stable behaviour. Figure 2 compares the values of the perturbation halving times for these stable orbits as a function of the initial distance from the system barycenter. Although the DPOs show the lowest values, these are obtained for orbits at close range from the surface of Didymain, where higher order gravitational harmonics (not accounted for in the CRTBP) may have a significant influence on the stability of the motion. On the contrary, the halving time of the DROs decreases as they get closer to Didymoon as a combined effect of the reduced value of the SI and of the shorter time-scale for the motion.

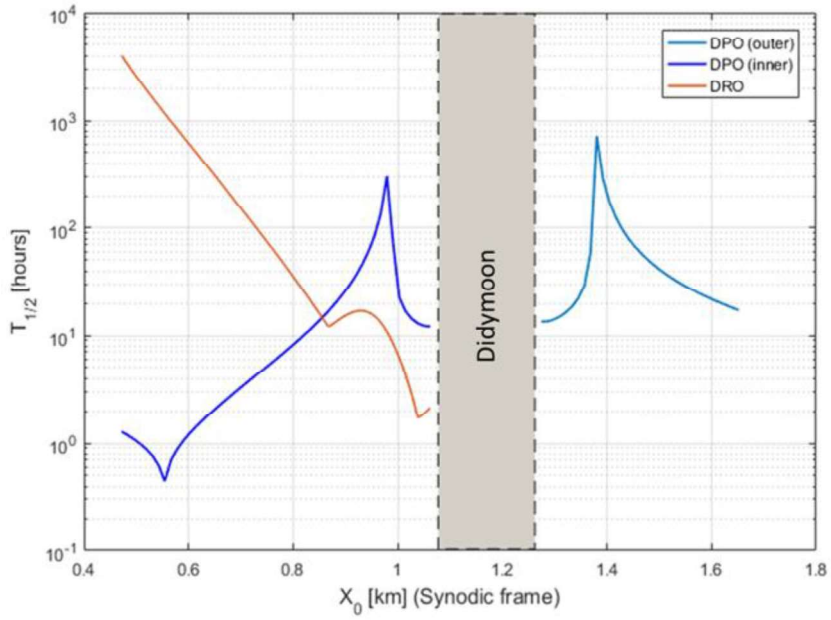

Figure 2 Perturbation half-time for stable orbits as a function of the initial x-coordinate in the Synodic reference frame. The grey region represents the surface of Didymoon.

Both orbital families show maximum distances from Didymoon below the value of $3\ km$ required for a continuous use of the RNH as laser altimeter and particle analyser. However, as shown in Figure 3, the DROs remain on average closer to Didymoon with respect to the DPOs, increasing the likelihood of crossing the ejected dust plume along their trajectory.
This combination of stability and close range makes the DROs the most suitable candidates for an eventual rendezvous with Didymoon after DART's impact. The outer DPOs might represent instead a valid option as injection orbits right after DustCube deployment and will be further investigated in section 3.8.

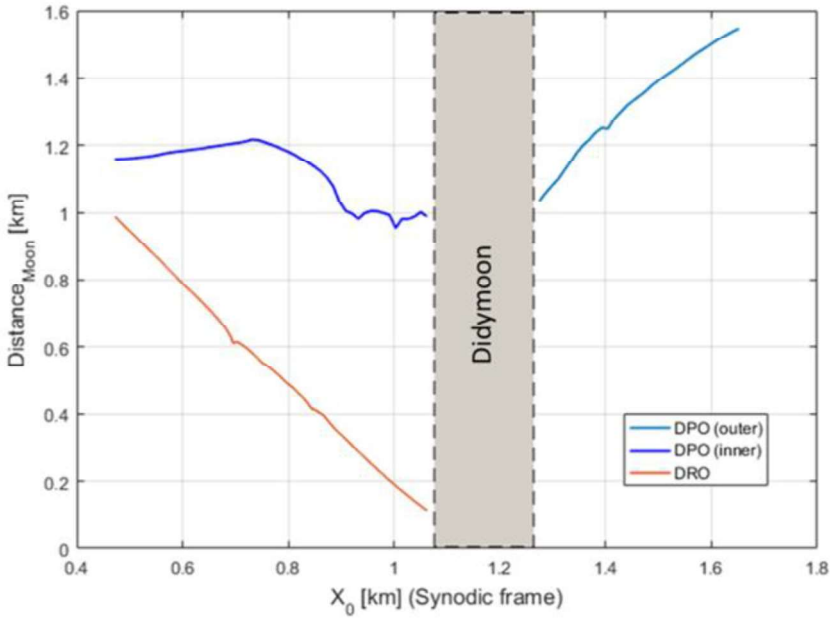

Figure 3 Mean distance from Didymoon barycentre along stable orbits as a function of the initial x-coordinate in the Synodic reference frame. The grey region represents the surface of Didymoon.

3.5 Preliminary concept of operations

According to the previously defined approach, a preliminary Concept of Operations (CONOPS) was outlined, which includes a baseline orbital strategy, together with two different alternatives based on the level of risk and on the likelihood of crossing the ejected dust plume during proximity operations. All the alternative strategies share the same Pre-Impact phase, which consists in the insertion of the s/c into a parking orbit at the Lagrangian point L_4.

For the impact operational phase, the following three alternatives are envisaged: 1) operations are performed while remaining at parking orbit; 2) DustCube performs a rendezvous with Didymoon and is inserted in a high altitude DRO at an average distance of roughly $300\,m$ from the surface; 3) DustCube performs a rendezvous with Didymoon and is inserted in a low altitude DRO at an average distance of roughly $100\,m$ from the surface. The last two options correspond to the orbits that have shown the most stable behaviour when integrated numerically into the ephemerides' model (Section 3.6). However, it can be observed that they are also close to the locations of minima for the stability index and perturbation half-time (see Figure 2), meaning that the overall stability characteristics of the DROs are retained in presence of perturbing effects.

Table 1 Characteristic parameters for the proposed orbits derived from the CR3BP: initial position (X_0) and velocity (V_0) in the synodic RF, orbital period (T), perturbation half-time $(T_{1/2})$ and average distance from Didymoon (D_{avg})

Orbit	$X_0[km]$	$V_0[cm/s]$	$T\ [h]$	$T_{1/2}\ [h]$	$D_{avg}[m]$
L_4	$[0.579, 1.022, 0]$	$[0, 0, 0]$	11.92	/	~ 1192
DRO (high)	$[0.802, 0, 0]$	$[0, 12.6, 0]$	10.1	34.13	486
DRO (low)	$[1.003, 0, 0]$	$[0, 7.72, 0]$	5	6.18	187

3.6 Validation in the High Fidelity Ephemerides model

The proposed CONOPS approach was validated by integrating the s/c trajectories inside the so-called High Fidelity Ephemerides Model (HFE), which is in agreement with the latest Didymos reference model available at the time of the present study. All of the trajectories were integrated using JPL's Mission-Analysis, Operations and Navigation Toolkit Environment (MONTE) software available at the Radio Science and Planetary Exploration Laboratory of the University of Bologna, currently used for the operations of all NASA's space missions managed by JPL (Evans et al., 2016) and for radio science data analysis (Tortora et al., 2016).

The dynamical setup of the HFE can be divided into three main sections: 1) barycentre motion, 2) relative motion of the two primaries and 3) DustCube motion about the system barycentre.

For the motion of the system barycentre, a Keplerian orbit about the Sun was considered, whose initial orbital parameters are taken from the JPL Small-Body Database (https://ssd.jpl.nasa.gov/sbdb.cgi)

For the relative motion of the primaries, Didymoon's trajectory was integrated numerically for a time span covering the expected mission duration and starting from the initial conditions shown in Table 2. The dynamical model for the relative motion included: 1) Point-mass gravity due to the Sun, the Solar System planets, the Moon and Pluto; 2) Gravity field of Didymain, which is modelled with a uniform density polyhedral shape (Werner & Scheeres, 1996). The motion of Didymain is obtained by combining the position of the barycentre with that of Didymoon.

Table 2 Didymoon's orbital parameters (J2000 Ecliptic frame) at 08/08/2022

Orbital Parameter	Unit	Value
a	km	1.18

e	-	0.0
i	deg	174
Ω	deg	220
ω_0	deg	0.0
M	deg	0.0

DustCube trajectories were integrated numerically starting from a series of ad-hoc initial conditions in the synodic reference frame (see Table 1) and considering: 1) Point-mass gravity of the Sun, the Solar System bodies, the Moon, and Pluto; 2) Gravity field of Didymain, which is modelled with a uniform density polyhedral shape; 3) Gravity field of Didymoon, which is modelled as a tri-axial ellipsoid of uniform density; 4) Solar Radiation Pressure (SRP), assuming a simplified shape for the s/c. In particular, only the J_2 and $C_{2,2}$ components were considered for the gravity field of Didymoon, where the numerical expressions are deduced from (Bills et al., 2014):

$$J_2 = \frac{\frac{2\pi}{15}\rho abc(a^2 + b^2 - 2c^2)}{MR^2} \quad (5)$$

$$C_{2,2} = \frac{\frac{\pi}{15}\rho abc(a^2 - b^2)}{MR^2} \quad (6)$$

Figure 4 shows the orbit obtained by integrating the s/c trajectory for a time span of two months, starting from the initial conditions of the L_4 equilibrium point. As it can be seen, the orbit remains confined within a narrow region around the Lagrangian point, suggesting that stability may be preserved even in the presence of perturbing effects and thus confirming the feasibility of the L_4 orbit strategy for the parking phase.

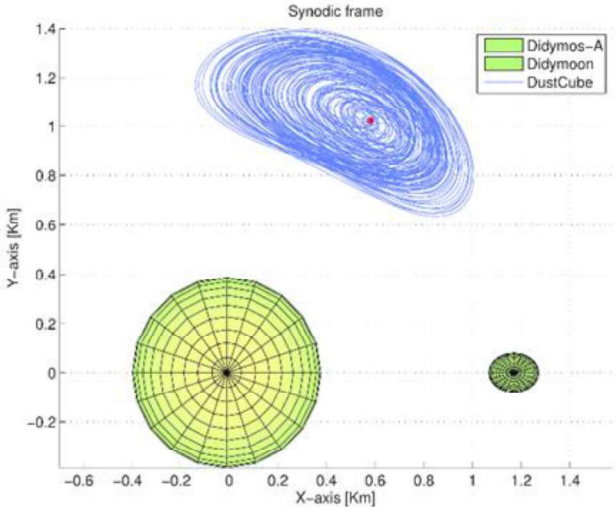

Figure 4 L4 parking orbit in the HFE model as seen in the synodic reference frame. The integration time span is two months, starting from the 8th of August 2022

Figure 5 shows the orbit that is generated using as initial conditions the low altitude DRO reference state and integrating the s/c trajectory for two weeks. Again, the osculating trajectory remains confined within a relatively narrow region around the reference solution, showing that the stable behaviour of the baseline orbit is preserved.

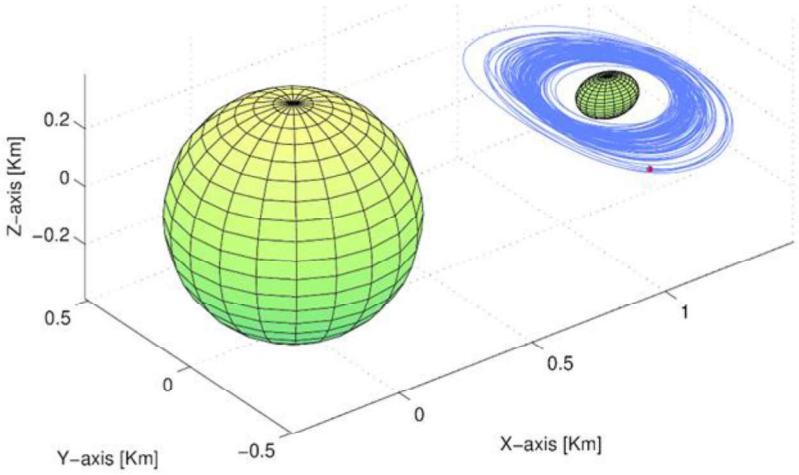

Figure 5 DRO orbit in the HFE model as seen in the synodic reference frame. The integration time span is two weeks, starting from the 8th of August 2022

3.7 Sensitivity to state errors

In order to assess the sensitivity to Orbit Determination and Control System (ODCS) errors, a series of uniformly distributed state errors were added to the initial conditions at the L_4 parking orbit, and trajectories were integrated numerically in the HFE model for a time span of one week. This time interval is assumed as a conservative order of magnitude estimation of the time required to complete ground-based orbit determination and perform a correction manoeuver. It is therefore important that the orbit does not depart significantly from the baseline during this time interval, so that the s/c can still survive in case of failure of the autonomous ODCS. An ad-hoc Figure of Merit (FM) was used to assess the stability of the orbit, which consist in the difference between the maximum and minimum distances from Didymain over a single orbital period:

$$FM = \frac{(d_1)_{MAX} - (d_1)_{min}}{2} \qquad (7)$$

Figure 6 shows the values of the FM as a function of the initial in-plane state components error, which provide the strictest requirements. This was expected, since the gravity field is almost symmetric with respect to the {*x* - *y*} plane, and therefore initial errors in the *z* direction only cause a periodic out-of-plane oscillatory motion. It is also interesting to observe that the highest sensitivity to velocity errors occurs along a direction that is tangential to the orbital motion, while the highest sensitivity to position errors occurs in the perpendicular direction.

The main outcome of this analysis was the estimation of reference values for the target ODCS accuracy, which were used in subsequent phases of the study, such as the ΔV budget computation (see Table 3). In particular, maximum position errors of $10\,m$ and velocity errors of $5\,mm/s$ are required to allow for safe operations.

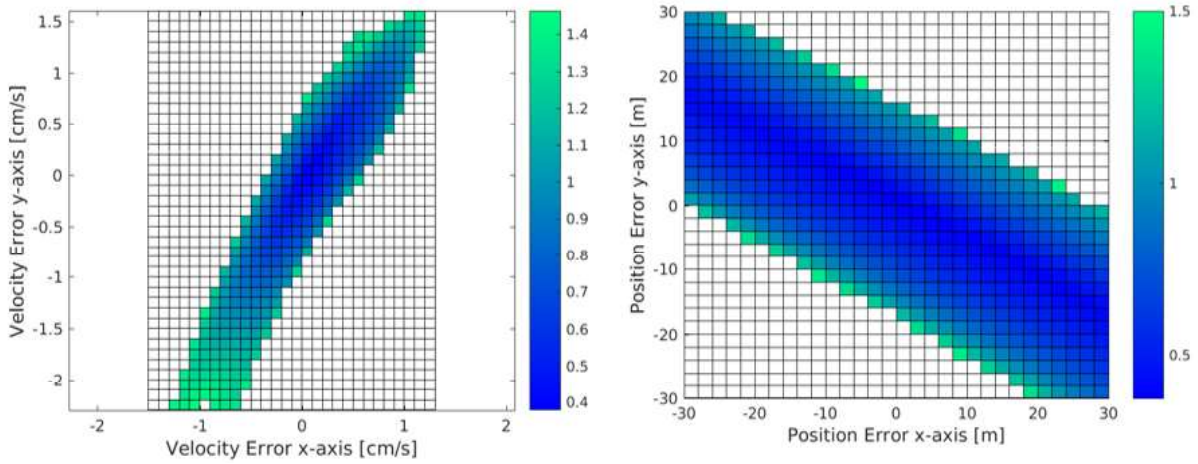

Figure 6 FM values for the L_4 parking orbit, against velocity errors (left figure) and position errors (right figure) in the {x-y} plane. Low values of the FM (blue) represent the most stable orbits. The white squares represent the initial conditions for which the end-time is not reached (the s/c escapes the system or crashes on the asteroids' surface).

3.8 Injection strategy

Given the many uncertainties regarding AIM's operations and its admissible trajectories during the Payload Deployment Phase (PDP), DustCube deployment represents one of the most critical aspects of this preliminary mission design.

The first issue that was addressed is the choice of a suitable injection orbit to be employed during the commissioning phase, which was conservatively assumed to last for 1 week. During this time, the s/c must survive without performing any SK manoeuvre while still remaining bound to the system.

Given their stable nature, which is preserved even for high values of the initial semi-major axis, the DPOs were considered as possible injection orbits and were integrated in the HFE dynamical model to verify their stability. The integration was performed for a time span of one month, starting from the initial conditions derived in the CR3BP, and would stop as soon as the s/c would exit from a "safe region" between $1.5\ km$ and $10\ km$ from the system barycentre. Figure 7 shows that a residence time comparable with the duration of the commissioning phase can be obtained for a wide range of initial conditions. In particular, a baseline orbit starting from $x_0 = 4\ km$ has been assumed in the following analysis.

The next issue that was addressed is represented by the injection constraints of the deploying mechanism onboard the AIM s/c (see point 5 of section 3.1), which only allows for deployment speeds down to $5\ cm/s$ with an accuracy of $\pm 1\ cm/s\ (1\sigma)$.

A possible solution, would be to deploy DustCube starting from an inclined orbit, and employing the injection speed as an impulsive manoeuver for a change of inclination. This approach has the advantage of having the injection velocity aligned in the out-of-plane direction, with respect to the orbital motion, where a lower sensitivity to velocity errors was observed (see section 3.7).

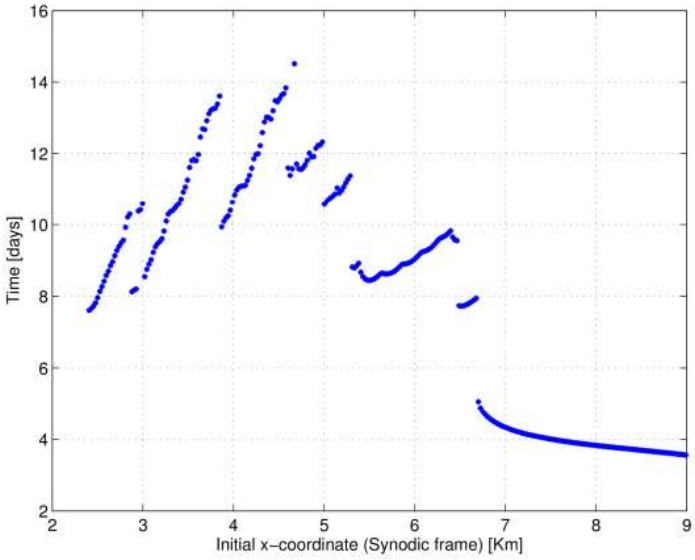

Figure 7 Residence time inside the [1.5 km, 10 km] region for DPOs as a function of the initial semi-major axis

By assuming an injection velocity of $5\ cm/s$ and an initial semi-major axis of $4\ km$, we can compute the required inclination off the Didymos orbital plane, corresponding to a value of 30.9^o.

A set of 1000 Monte Carlo simulations was run in the HFE dynamical model, starting from the initial conditions of the baseline DPO and adding random injection velocity errors in the direction perpendicular to the orbital plane, having standard deviation equal to the accuracy of the deploying mechanism. All the integrated trajectories showed a residence time of more than one week inside the "safe region", proving the soundness of the proposed injection approach. It is worth noticing that the current analysis does not take into account the estimated accuracy of AIM's ODCS during the PDP, which is expected to represent only a second order contribution to the deployment errors.

3.9 Station-keeping at parking orbit

The estimation of the Station-Keeping (SK) ΔV budget at parking orbit posed a challenging task, which departs from the common SK approaches that are found in literature (Folta et al., 2010). Indeed, simulations of the L_4 parking orbit in the HFE model suggest that, for small errors in the initial conditions, the s/c is likely to stay in the vicinity of the equilibrium point. In this case, mission constraints are still satisfied because the s/c remains at close range from Didymoon to allow for remote sensing. Therefore, targeting a specific pre-defined orbit may represent an unnecessary effort. Considering these factors, an energetic approach was designed for the SK ΔV budget estimation that makes use of the Jacobi constant. A series of Monte Carlo simulations were performed, by introducing zero mean Gaussian state errors and integrating the s/c trajectories in the HFE model for a timeframe of two months. In addition to random state errors, uniformly distributed variations of the SRP scale factor were introduced to take into account variable factors like the s/c orientation and the optical properties of the materials. Depending on the magnitude of the initial errors, trajectories would depart from the equilibrium point at different rates and reach a pre-defined boundary where the SK manoeuvers would take place. This boundary region was chosen as a tri-axial ellipsoid centred at the L_4 point, with principal axes of the type $[R, R/2, R/2]$, and having its semi-major axis along the direction of highest sensitivity to the velocity errors (i.e. tangential to the orbital motion).

Once reached the boundary, the required ΔV to bring the s/c back to the equilibrium state will depend on the employed transfer orbit. However, it is possible to estimate a lower bound for the ΔV as a function of the difference in the JC values between the s/c state at the border crossing and the one at the equilibrium point, whose value is fixed and equal to $JC_{eq} = 2.99$. Following this approach, three Monte Carlo simulations were performed by integrating 1000 trajectories each, with different errors in position, velocity, and SRP, as shown in Table 3.

Table 3 Error modelling for the Monte Carlo simulations

Error components	Unit	Best	Nominal	Worst
Velocity errors (1σ)	mm/s	1.25	2.5	5
Position errors (1σ)	m	2.5	5	10
SRP scale factor (uniform)	-	[0.9 - 1.1]	[0.8 - 1.2]	[0.6 - 1.4]

Figure 8 shows the estimated station-keeping ΔV per day of operations as a function of the equivalent radius of the border ellipsoid R, assuming nominal values for the state errors. At each radius, the required ΔV was estimated by computing a weighted average of the single ΔV_i for the sample orbits, using the expression in (8), where t_i is the elapsed time at border crossing.

$$\Delta V = \sum_{i=1}^{N} \frac{\Delta V_i}{t_i} \qquad (8)$$

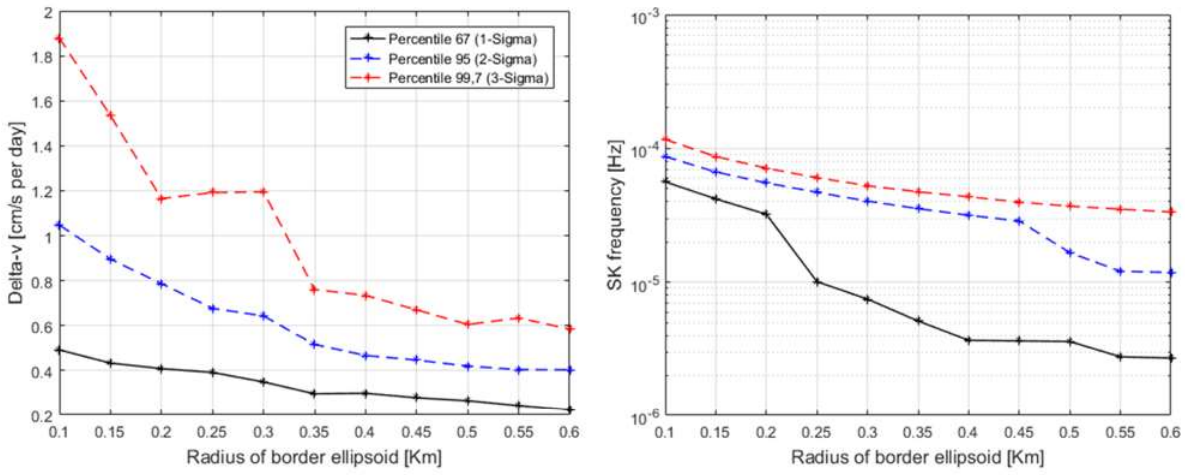

Figure 8 Station-keeping ΔV (left) and frequency (right) at L_4 for the nominal OD accuracy case. The three coloured lines, represent the 67th, 95th and 99.7th percentiles, meaning that by choosing the ΔV values corresponding to these lines, we have the 67%, 95% and 99.7% confidence that the single ΔV_i samples will be lower than the estimated value.

By looking at Figure 8, it can be seen that the required ΔV drops off as the border ellipsoid gets wider. This was expected, since more frequent manoeuvers are required to keep the s/c within narrow boundaries. Depending on the maximum allowable s/c drifts from the equilibrium point and on the overall ΔV budget for the mission, a trade-off may be performed at later stages of the mission design to choose the best SK manoeuvring locations. Table 4 summarizes the estimated ΔV values in all three alternative cases. As expected, the ΔV increases as the initial state errors increase.

3.10 Station-keeping at proximity orbits

A different SK approach was employed for the proximity operations at rendezvous with Didymoon, more specifically a loose SK strategy, which aims at keeping the s/c within the desired *region of space* while allowing for some occasional drifting (see Figure 9). Since the requirement of the dust-plume tracking does not pose strict conditions on the exact crossing location, this represents a suitable option to reduce the required ΔV with respect to tight SK strategies that target a pre-defined baseline orbit (Folta et al., 2010).

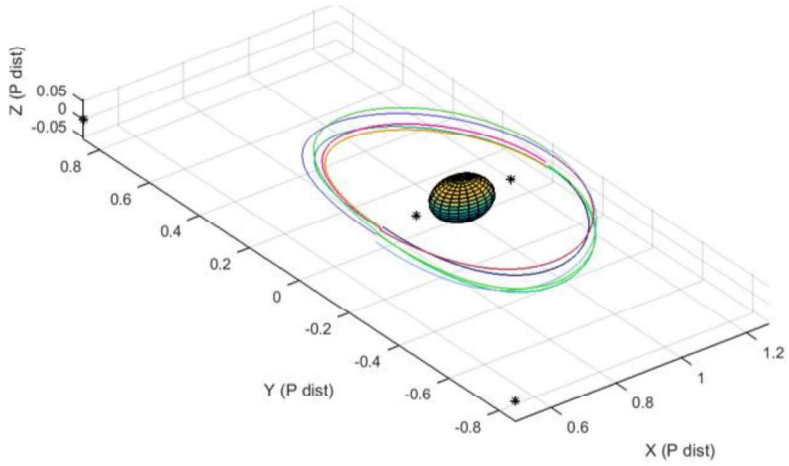

Figure 9 Representation of loose station-keeping strategy for the high altitude DRO option

The specific SK method is the one described by (Parker & Anderson, 2013), which is suitable for simple periodic orbits. The idea is that a given SK manoeuvre is designed to target a trajectory that pierces the $\{x-z\}$ plane orthogonally at either the next or a subsequent crossing. This ensures that the s/c remains in the vicinity of its libration orbit for at least some time, depending on the magnitude of the ODCS errors. A MATLAB® software routine was implemented that makes use of the same differential correction algorithm described in Section 3.4. A Monte Carlo simulation was performed, by introducing initial random state errors and integrating the s/c trajectories in the CR3BP model for two successive $\{x-z\}$ plane crossings. The differential corrector was then applied in order to obtain a trajectory that pierced the $\{x-z\}$ plane with zero velocity along the x-axis, meaning that the corrected trajectory retained its periodicity. After the corrected initial state had been identified, a random manoeuvre error of $\sigma_{man} = 0.1\ mm/s$ (corresponding to a conservative 10% of the average ΔV correction for the baseline case) was introduced. The whole process was then repeated for a number of five SK manoeuvres (and thus revolutions), each time reintroducing the estimation and manoeuvring errors.

According to this design, each SKM is performed once per orbit at an $\{x-z\}$ plane crossing and targets a future crossing. There may be benefit from placing the SKMs at different points along the orbit, or even allowing the time interval between manoeuvres to vary. However, these strategies have not been explored for simplicity. Table 4 summarizes the obtained values for the station-keeping ΔV in the presence of the random ODCS errors described in Table 3. The reported values for the proximity operations are obtained by averaging a total of 200 Monte Carlo simulations (corresponding to 1000 SK manoeuvres overall). Note that the differential correction method failed to converge for the DROs with worst-case errors: this is an indication that more frequent correction manoeuvres would be required for station-keeping in such scenarios.

Table 4 ΔV estimation summary for the three alternative scenarios. For parking at L_4, the reference value is obtained with the radius of the border ellipsoid at 0.45 km and considering the 95th percentile.

	Unit	Best	Baseline	Worst

Parking at L_4	*mm/s per day*	1.86	4.84	12.16
High alt. DRO	*mm/s per day*	1	4.21	Failed to converge
Low alt. DRO	*mm/s per day*	2.12	4.35	Failed to converge

3.11 ADCS design

A momentum biased, 3-axes stabilized platform is proposed for DustCube, featuring two redundant star-trackers, a triaxial gyroscope and 6 sun sensors for attitude determination. Attitude control will be achieved with the use of three reaction wheels for torque compensation and slewing manoeuvres and a series of cold gas thrusters for detumbling and wheels' desaturation. The preliminary reaction wheel sizing in Table 5 shows that the dominant contribution in terms of torque authority is due to the slew manoeuvers and that the total torque requirements are compatible with COTS CubeSat-sized actuators. An estimation of the frequency of desaturation manoeuvers was then derived by simply dividing the assumed angular momentum storage capacity of $6 \cdot 10^{-3}\mathrm{Nms}$ by the maximum disturbance torque estimated for each mission segment. A value of roughly one manoeuver every week of operations was estimated, which is two orders of magnitude lower than the estimated frequency of the SK manoeuvres at the L_4 parking orbit.

Table 5 Reaction wheels' sizing

	Maximum torque (Nm)	**Comments**
Disturbance rejection	2.05×10^{-8}	This includes contributions from Gravity Gradient and SRP torque (assuming a *5 cm* offset between COP and COG)
Slew	6.25×10^{-5}	Assuming a maximum angular velocity of *1.5 deg/s*
Total	**8.13×10^{-5}**	With 30% safety margin

3.12 Total ΔV budget

Table 6 summarizes the overall ΔV budget estimation for the DustCube mission for the three alternative scenarios described in Section 3.5 and assuming accuracies of the ODCS as shown in Table 3. These values represent the sum of all the contributions coming from the orbital control and from the attitude control. In particular, the ODCS contribution includes: transfers from and to the parking orbit at L_4, SK at parking orbit or at proximity orbit (depending on the mission scenario) and transfer from and to the proximity DROs. On the other hand, the ADCS contributions include: detumbling after DustCube injection and wheels momentum unloading. This last contribution was obtained neglecting additional orbital ΔV corrections due to the possible uncoupling of the attitude control thrusters, which seems reasonable, given the low frequency of desaturation manoeuvres.

The overall mission ΔV, slightly more than 2 m/s, is fully compatible with state-of-the-art cold gas micro-propulsion systems designed for 3U platforms[2].

Table 6 Total ΔV budget summary (with 30% margin)

CONOPS	**Unit**	**Best**	**Baseline**	**Worst**
Alt. 1	m/s	0.54	0.98	1.96
Alt. 2	m/s	0.74	1.18	2.10
Alt. 3	m/s	0.93	1.19	2.11

[2] See e.g. Gomspace NanoProp, capable to provide a total specific impulse of $40\ Ns$ using Butane as propellant.

[3] See e.g. Hyperion Technologies RW210, capable of providing a maximum torque of $0.1\ mNm$ and a total angular momentum storage of $6 \cdot 10^{-3}\mathrm{Nms}$

4 Optical Navigation

4.1 Introduction

The orbital analysis described in Section 3 relies on the assumption that the ODCS can control the s/c state with accuracies that are comparable with the ones shown in Table 3 to keep the probe in the proximity of the reference orbit. To verify the rationality of this assumption, it was therefore necessary to propose a preliminary layout for the ODCS and to estimate its accuracy. However, a detailed characterization of the ODCS accuracy would require the implementation of a full navigational filter and the setup of a simulating environment with detailed shape models for the asteroids, which is beyond the scope of a preliminary Phase-A study. For this reason, a simplified analysis based on a pure geometrical approach was performed to address the overall feasibility of the proposed navigation approach and to drive its implementation by setting upper bounds to the position error estimations.

4.2 Optical navigation principles

DustCube orbit determination concept mainly relies on the 3D localization principle described by (Bhaskaran et al., 1996) and shown in Figure 10. The general 3D localization concept relies on the observation of nearby objects, referred to as beacons, whose relative positioning is already known, to infer the s/c position with respect to the beacons. By shuttering an image of a beacon, its position in the camera Field-Of-View (FOV) determines a Line-Of-Sight (LOS) direction to that beacon on which the s/c must lie. Two such LOS directions recorded simultaneously place the s/c position at the intersection of the vectors. Once the s/c position is known in the local synodic reference frame, its position can also be determined in the inertial reference frame using a star tracker for precise attitude determination.

Since the six degrees of freedom for the s/c state need to be constrained, at least other two LOS measurements are required to get an estimate of the velocity. Individual LOS images are then taken over some interval of time and the entire data set is processed in a filter to determine the s/c state.

This approach is particularly suited for the present case, given the binary nature of the Didymos system, where two close range beacons are always visible from the s/c (except in case of occultations).

The accuracy of this method depends on several factors, which will be considered in the upcoming analysis: 1) the ability to find the exact centre of mass (COM) of the asteroids, which depends on the image processing algorithms, on the resolution of the cameras and on the models that are used to approximate the asteroids' shape; 2) the distance between the s/c and the two beacons; 3) the observation geometry; 4) the accuracy of the asteroids' ephemerides.

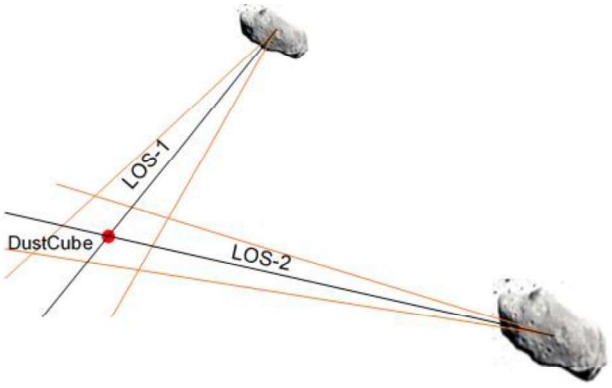

Figure 10 Principles of 3D localization using two LOS measurements.

4.3 DustCube ODCS layout

Given the operational scenario for DustCube, the following ODCS concept has been proposed:

1) Orbit determination will be performed using a dual Infra-Red (IR) camera configuration for the simultaneous estimation of the LOS vectors to the asteroids. IR was preferred in lieu of the visible part of the spectrum so that the ODCS performances are not affected by illuminating conditions and shadowing effects. A separate star-tracker is employed for attitude determination, which will by mounted with its camera FOV along the out-of-plane direction so that its measurements are not affected by the asteroids' brightness.

2) Orbital control will be achieved with the use of a Cold-Gas propulsion system having its main thruster at the rear end of the 3U structure. A series of 12 smaller thrusters will be installed to gain 6 DoF capabilities, which will also be used for detumbling and desaturation of the reaction wheels.

Figure 11 shows the proposed configuration, which currently foresees an angular separation of 60° between the two cameras. This corresponds to the average angular separation between the two asteroids at the L_4 parking orbit, for which this configuration is optimal. However, the wide field of view of the pre-selected cameras, ranging up to $69°$, still allows for some flexibility by providing coverage of the primaries over a wide range of geometrical conditions.

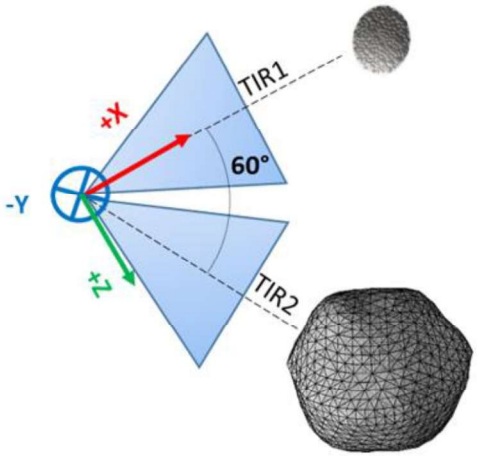

Figure 11 Proposed IR cameras' configuration (left.

4.4 Geometric simulation setup

To preliminary assess the magnitude of the ODCS errors, a MATLAB® software simulating the geometrical orbit determination was developed and tested during the course of the present study. This model assumes that the orbit determination is performed directly through the observation of the LOS vectors of the two asteroids in the s/c body frame, using the triangulation technique described in Section 4.2. In the following analysis we will also assume that the IR cameras are able to follow the motion of the primaries with complete coverage over the orbit and that the Centre Of Brightness (COB) of the primaries always lies at the centre of the cameras' FOV.

Synthetic camera measurements were generated by corrupting the exact LOS unit vectors of the asteroids with the random errors that are described in Table 7, and centring these vectors to the noisy asteroids ephemerides. Then, the algorithm computed the s/c position as the midpoint of the segment of closest approach between two lines stemming from the centroids of Didymoon and Didymain that, in general, do not cross. The estimated error for the measurement was then defined as the difference between the reference position of the s/c taken from the true ephemerides, computed in the CR3BP, and the position estimated with this algorithm.

It is important to point out that most of the error sources described in Table 7 represent conservative estimations and are taken as constant throughout this analysis. The only exception is represented by the COB to COM error, which is left to vary in order to find the maximum value which still allows to

reach the target accuracy. Values between 1% and 4% of the same angular semi-aperture of the asteroid as seen from the s/c, were considered, in agreement with (Statsny and Geller, 2008).

Table 7 Modelling of the ODCS error sources

Source	Magnitude	Comments
Absolute Knowledge Error (AKE)	$\sigma = 0.1°$	Error in the knowledge of the absolute s/c attitude, modelled using three successive rotations about the coordinate axes.
Misalignment Error (ME)	$\sigma = 0.1°$	Error in the knowledge of the cameras' alignment, modelled using three successive rotations about the coordinate axes.
Centre of Brightness to Centre of Mass (COB to COM)	$\sigma = \mathrm{f}(\alpha)$	Angular displacement between the COB of the beacon and the true COM location.
Asteroid ephemerides' error	$\sigma = 5$ m	Error in the inertial asteroid position. Only applied to Didymoon. Assumed conservatively higher than what expected, i.e. $1.1\ m$ after DCP and $0.55\ m$ after PDP (Zannoni, et al., 2017)

4.5 Estimated accuracy for orbit determination

The results presented hereafter show the values of the estimated position errors in two alternative forms. The first one is represented by the Root Mean Square (RMS) errors obtained along the three coordinate axes. The second one is represented by the radius of the equivalent confidence sphere around the true position, whose definition starts from that of the confidence ellipsoid, which is the ellipsoid where a certain percentage of an ensemble will lie. Considering as an example a probability value of 95%, the confidence ellipsoid is the region (around the true position) where 95% of the position estimates are confined. By calculating the volume of this ellipsoid, it is then possible to find the radius of a sphere having an equivalent volume, which is assumed as a good single-value representation of the position error. This assumption is verified only if none of the RMS errors for the separate components is significantly larger than the others, corresponding to the case of a highly elongated ellipsoid.

Figure 12 shows the estimated RMS errors at the L_4 parking orbit, assuming values for the COB to COM errors of 2% and 4% respectively. In the former case, the errors remain confined within an acceptable value of $10\ m$, while in the latter case there is a sudden increase in the LOS direction error. This is probably due to the significant FOV extension of Didymain, which makes the system more sensitive to COM location errors. It is also observed that the LOS component of the position is the dominant source of uncertainty, with the other two components being dominated by the asteroid ephemerides' errors, which set a lower limit to the accuracy of the system.

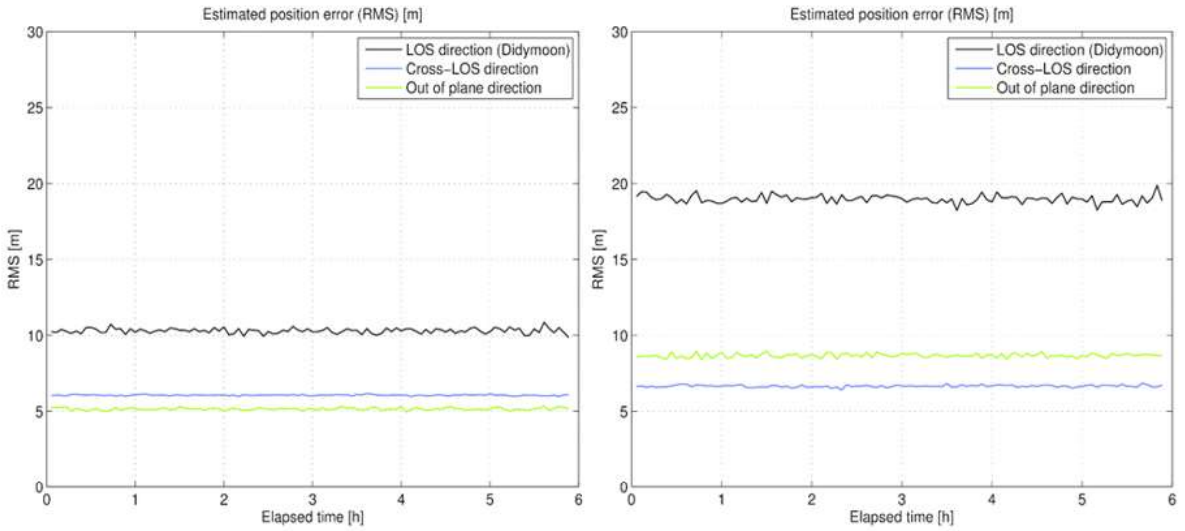

Figure 12 Position error RMS at L4 parking orbit, for a COB to COM error of 2% (left) and 4% (right).

Figure 13 shows the RMS error for the proximity operations at the high altitude DRO, with a COB to COM estimation error of 2%. It can be observed that the LOS component of the position error, which is again the dominant source of uncertainty, is highly dependent on the angular separation between the two primaries and shows an exponential rise when the s/c and the asteroids are in conjunction. However, the dynamics of the DROs is such that most of the orbital period is spent in regions with favourable geometry, so that the errors remain below the pre-defined boundary for a significant portion of the orbital period. During periods of unfavourable geometric conditions, the s/c will thus need to rely on the navigation filter for orbit propagation or on alternative ranging measurements for the estimation of the LOS distance from Didymoon.

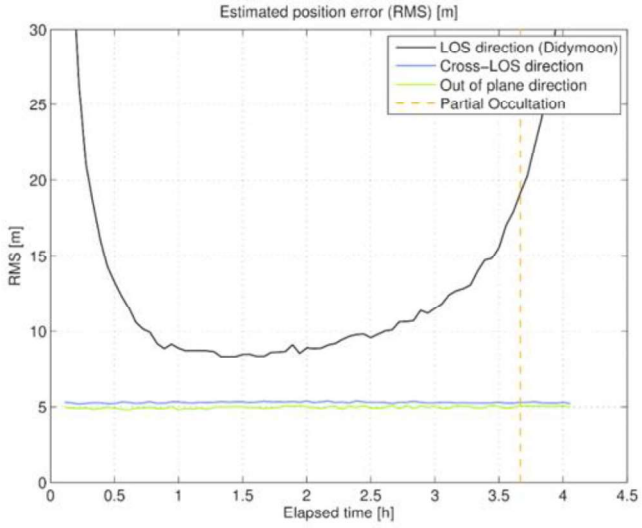

Figure 13 Position error RMS for a high altitude DRO, for a COB to COM error of 2%

Finally, Figure 14 shows the radii of the equivalent confidence spheres, for a COB to COM error of 2% for the proximity operations at the high altitude DRO. It can be seen that, under these assumptions, it is actually possible to remain within the defined threshold of 10 m with a confidence value of 95% (corresponding to a value of 2σ for normal distributions) for most part of the orbital period.

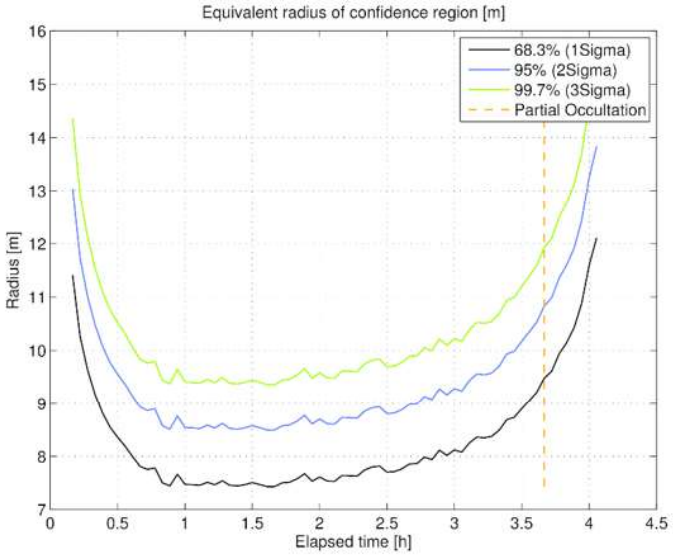

Figure 14 Radius of the equivalent confidence sphere for the high altitude DRO alternative, for a COB to COM error of 2%

Overall, the preliminary optical navigation analysis shows that the expected accuracies for the ODCS are consistent with the target values that were derived during the orbital analysis. However, in order to meet the desired accuracies the COB to COM error should remain within the acceptable limit of 2% of the FOV aperture. Hence, Limb-fitting techniques shall be implemented and coupled with accurate shape models for the asteroids (depending on the true shape of the bodies and on their level of irregularity). A great improvement in the ODCS accuracy may come from additional ranging information (w.r.t. Didymoon), derived from Limb-fitting of the IR images or LIDAR measurements exploiting the on-board laser component of the RNH. These techniques would in fact reduce the uncertainties in the LOS distance estimation, which represents the biggest error contribution for all mission scenarios. The implementation of a full navigation filter is also expected to improve the overall accuracy of the orbit-determination. Within the same analysis we expect to be able of addressing the issues of a more realistic duty cycle, which should include operational and maintenance requirements such as communications, solar panels orientation or thermal system management.

4.6 Computational burden

An assessment of the computational resources to be allocated for orbit determination, in terms of floating point operations (FLOPs) counting, was performed for the following tasks: 1) image processing and 2) orbit determination filter update. Preliminary results indicated that the biggest contribution to the computational burden is represented by the image processing algorithms, whose main steps are listed in Table 8.

Table 8 Computational resources for image processing

	Operations	Comments
Pre-processing (thresholding)	2×0.33 MFLOPs	Considering two IR images of size $640 \times 512\ px \approx (0.33\ Mpx)$
Edge extraction	2×10 MFLOPs	Based on an average of 30 FLOPS per pixel, typical for a Sobel convolutional operator.
Limb fitting	2×0.1 MFLOPs	Based on an ellipse least square fitting on a $640 \times 512\ px$ image

The estimated image processing burden, MFLOPs ≈ 21, is comparable with that of commercial CubeSat sized processors, e.g. the 23 MFLOPs/sec of a LEON-2 processor. By combining this information with the current baseline frequency for the OD filter image-measurement update, which

corresponds to ≈ 10^{-2} Hz, we have an indication of the overall feasibility of a real-time on-board implementation.

5 Concluding remarks

This paper provided an overview of the orbital analysis that was performed as a part of the preliminary design of the DustCube mission towards the Didymos system. Possible trajectories that exploit the binary nature of the system were obtained in the simplified CR3BP by using a differential correction method. Suitable orbital solutions in terms of stability and geometrical constraints were identified among these trajectories, and form the basis for the preliminary concept of operations. This currently foresees an initial parking orbit at the L_4 equilibrium point, followed by different possible scenarios, characterized by increasing levels of risk and operational complexity: continue orbiting at L_4 (low risk), transfer on high altitude DRO at roughly $300\ m$ from the surface of Didymoon (medium risk), or transfer to a low altitude DRO at roughly $100\ m$ from the surface of Didymoon (high risk). All the three alternatives retain their stability characteristics when integrated into a high fidelity ephemerides model and are consistent with the manoeuvring capabilities of a Cubesat platform in terms of total delta-v budget and of performances of the available attitude actuators. However, this result is strictly coupled with the overall performance of the orbit determination system, which is required to provide target position and velocity accuracies of $10\ m$ and $5\ mm/s$, respectively, to allow for safe operations.

Results of a geometrical OpNav simulation suggest that the target positioning accuracy can be achieved at parking orbit, provided that sufficiently accurate asteroid ephemerides are available and that the ODCS centre-finding algorithms are capable of maintaining the COB to COM error within an acceptable value of 2% of the asteroids' FOV extension. To this end, accurate limb fitting algorithms coupled with detailed shape models of the asteroids will be required for the COG estimation, as opposed to simple image centroiding. Conversely, the target accuracy can be reached for proximity operations only for a limited portion of the orbital period. In this case, additional information is required to improve the LOS distance estimation, which may come from laser altimetry (RNH) or from a scaling of the fitted limbs.

Future works will need to focus on the selection of some image processing techniques that are capable of providing the required accuracy in the COG estimation while limiting the computational burden for the OpNav, which was preliminarily estimated to be compatible with COTS micro-processors.

The implementation of a full navigation filter also represents a necessary step towards the validation of the proposed design and is the subject of current investigations from the authors. Simulations of the filter inside the HFE dynamical model will provide more accurate estimations of the overall ODCS accuracy and on the characteristic timescales for its convergence.

6 Acknowledgments

The research described in this paper was carried out at the University of Bologna, in the framework of ESA contract No. 4000115088/15/F/MOS "Asteroid Impact Mission (AIM) Cubesat Opportunity Payloads (COPINS)". The authors want to express their gratitude to all members of the DustCube consortium, and in particular to Fernando Aguado, Franco Perez Lissi, and Ricardo Tubio Pardavila from the University of Vigo and Gergely Dolgos from Micos Engineering GmbH. The support of all involved ESA personnel and in particular Ian Carnelli, Roger Walker and Borja Garcia Gutierrez is also greatly acknowledged. Special thanks go to Shantanu Naidu and Lance Benner from NASA/JPL

for making available their polyhedral shape model of Didymos primary prior to publication. The authors wish to acknowledge Caltech and the Jet Propulsion Laboratory for granting the University of Bologna a license to an executable version of MONTE Project Edition S/W.

7 References

Bhaskaran, S., Riedel, J. E., & Synnott, S. P. (1996). Autonomous optical navigation for interplanetary missions. In SPIE's 1996 International Symposium on Optical Science, Engineering, and Instrumentation (pp. 32-43). International Society for Optics and Photonics.

Bills, B. G., Asmar, S. W., Konopliv, A. S., et al. (2014). Harmonic and statistical analyses of the gravity and topography of Vesta. Icarus, 240, 161-173.

Broschart, S. B., Lantoine, G., & Grebow, D. J. (2014). Quasi-terminator orbits near primitive bodies. Celestial Mechanics and Dynamical Astronomy, 120(2), 195-215.

Chappaz, L., Broschart, S. B., Lantoine, G., & Howell, K. (2015). Orbital Pertubation Analysis near Binary Asteroid Systems. Presentation at AAS/AIAA Spaceflight Mechanics Conference, Williamsburg, VA. AAS 15-330.

Chappaz, Loic & Howell, Kathleen. (2014). Bounded Orbits near Binary Systems Comprised of Small Irregular Bodies. Presentation at AIAA/AAS Astrodynamics Specialist Conference. DOI: 10.2514/6.2014-4153.

Cheng, A. F., Atchison, J., Kantsiper, B., et al. (2015). Asteroid Impact and Deflection Assessment mission. Acta Astronaut. 115, 262–269. doi:10.1016/j.actaastro.2015.05.021

Cheng, A. F., Michel, P., Jutzi, M., et al. (2016). Asteroid Impact & Deflection Assessment mission: Kinetic impactor. Planet. Space Sci. 121, 27–35. doi:10.1016/j.pss.2015.12.004

Evans, S., Taber, W., Drain, T., Smith, J., Wu, H., Guevara, M., Sunseri, R., Evans, J., 2016. Monte: the Next Generation of Mission Design & Navigation Software, in: The 6th International Conference on Astrodynamics Tools and Techniques.

Folta, D., Bosanac, N., Guzzetti, D., Howell, K. C. (2015). An Earth–Moon system trajectory design reference catalog. Acta Astronautica, 110, 341-353.

Folta, D., Pavlak, T. A., Howell, K. C., et al. (2010). Stationkeeping of Lissajous trajectories in the Earth-Moon system with applications to ARTEMIS. In 20th AAS/AIAA Space Flight Mechanics Meeting, San Diego, California (presentation n. 10-113).

Godard, B., Budnik, F., Munoz, P., Morley, T. (2015). Orbit Determination of Rosetta Around Comet 67P/Churyumov-Gerasimenko, in: ISSFD. pp. 1–30. doi:10.1017/CBO9781107415324.004

Michel, P., Cheng, A., Kueppers, M., et al. (2016). Science case for the Asteroid Impact Mission (AIM): A component of the Asteroid Impact & Deflection Assessment (AIDA) mission. Adv. Sp. Res. 57, 2529–2547. doi:10.1016/j.asr.2016.03.031

Michel, P., Kueppers, M., Sierks, H., et al. (2017). European component of the AIDA mission to a binary asteroid: characterization and interpretation of the impact of the DART mission, submitted to Advances in Space Research, Manuscript Number ASR-D-17-00415R1.

Parker, J. S., & Anderson, R. L. (2014). Low-energy lunar trajectory design. John Wiley & Sons, Hoboken, New Jersey.

Scheeres, D. J. (1994), Satellite dynamics about asteroids. JPL Technical Report Server, 94-0254, (URI: http://hdl.handle.net/2014/32511)

Stastny, N. B., & Geller, D. K. (2008). Autonomous optical navigation at Jupiter: a linear covariance analysis. Journal of Spacecraft and Rockets, 45(2), 290-298.

Tortora, P., Zannoni, M., Hemingway, D., Nimmo, F., Jacobson, R.A., Iess, L., Parisi, M., (2016). Rhea gravity field and interior modeling from Cassini data analysis. Icarus 264, 264–273. doi:10.1016/j.icarus.2015.09.022

Werner, R. A., & Scheeres, D. J. (1996). Exterior gravitation of a polyhedron derived and compared with harmonic and mascon gravitation representations of asteroid 4769 Castalia. Celestial Mechanics and Dynamical Astronomy, 65(3), 313-344.

Zannoni, M., Tommei, G., Tortora, P., et al. (2017). Radio Science Investigations with the Asteroid Impact Mission, submitted to Advances in Space Research.

figure 1.png

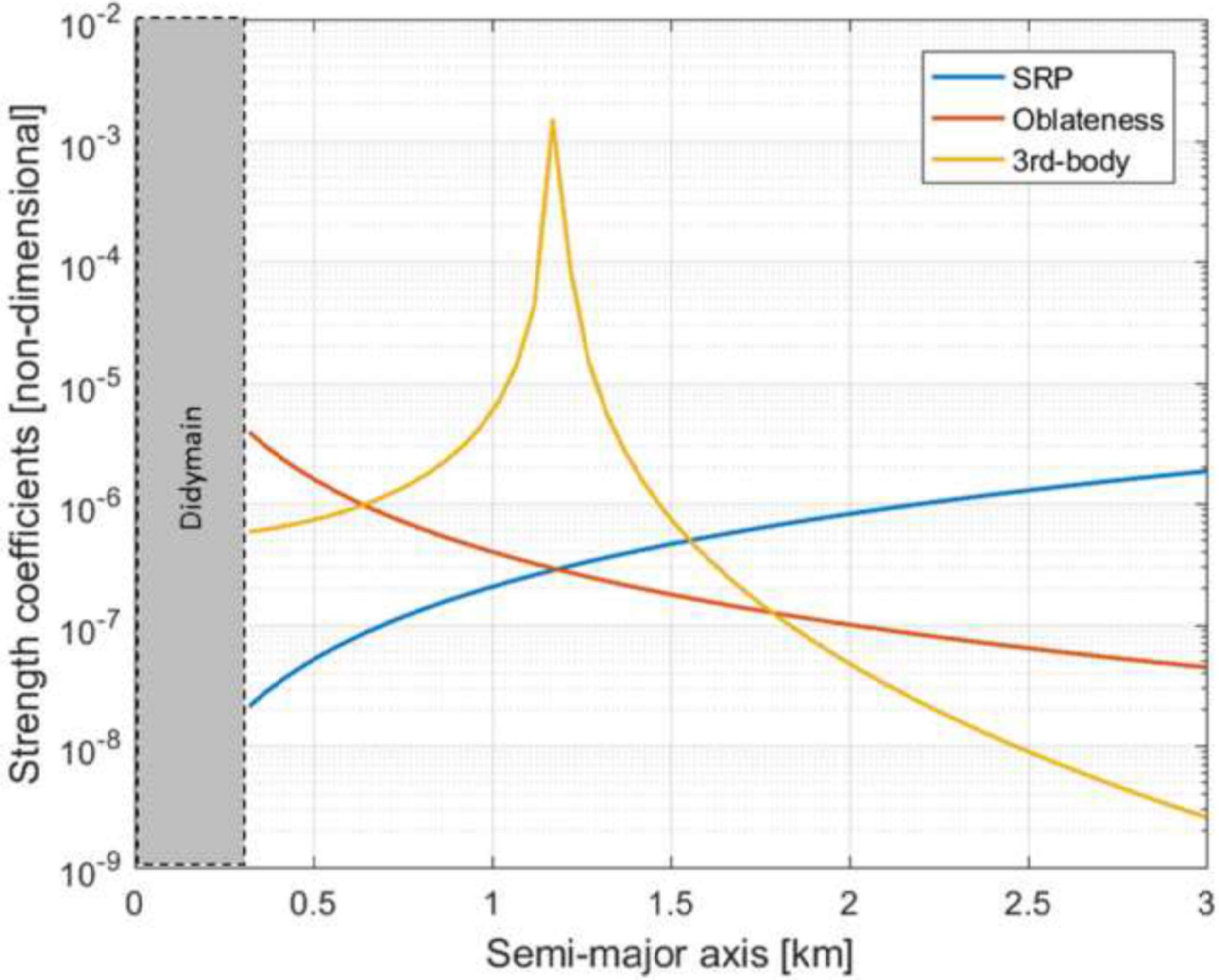
Strength coefficients [non-dimensional]
Semi-major axis [km]
Didymain
SRP
Oblateness
3rd-body
10^-2
10^-3
10^-4
10^-5
10^-6
10^-7
10^-8
10^-9
0
0.5
1
1.5
2
2.5
3

figure 2.png

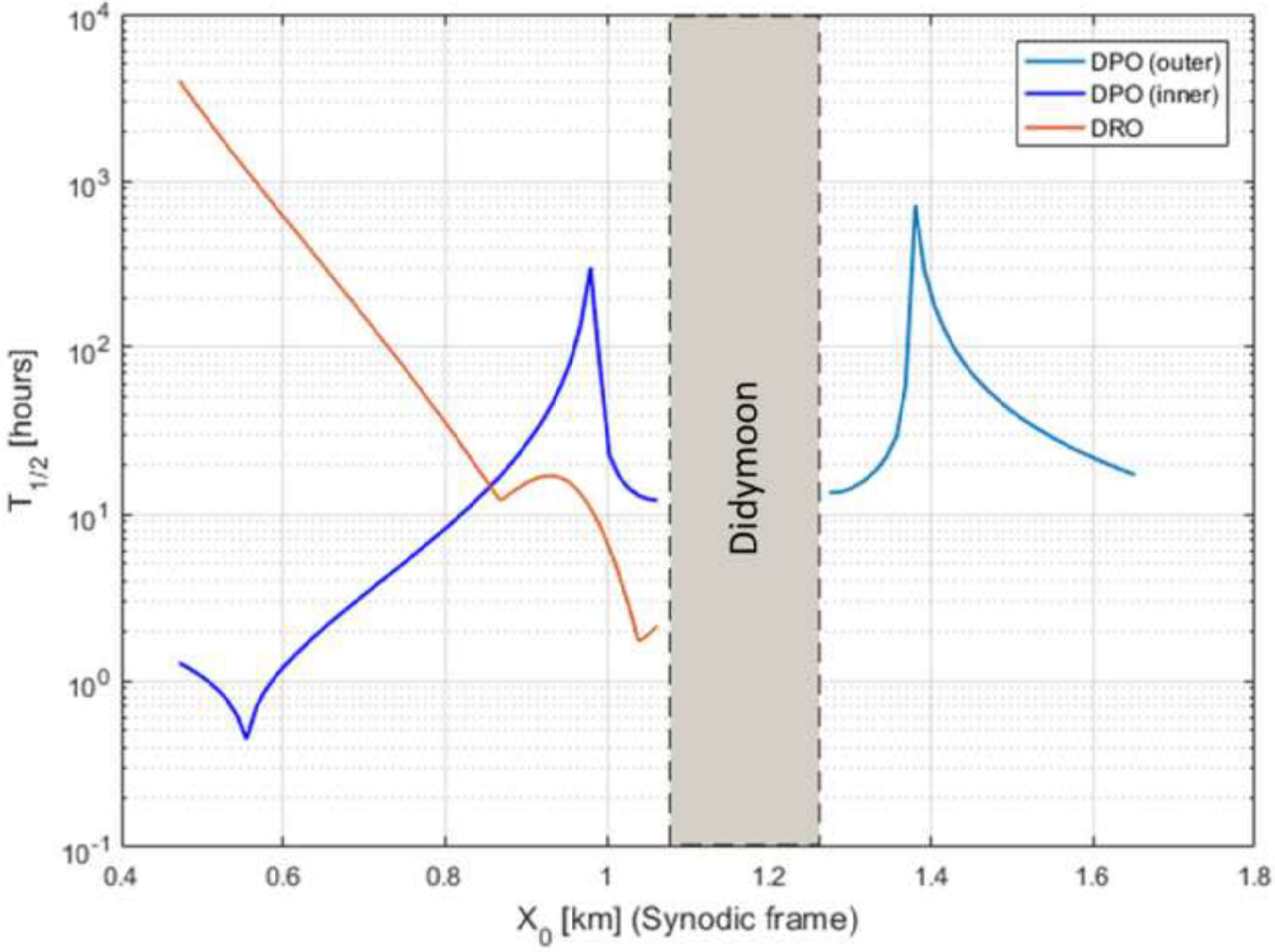
DPO (outer)
DPO (inner)
DRO
Didymoon
$T_{1/2}$ [hours]
X_0 [km] (Synodic frame)
10^4
10^3
10^2
10^1
10^0
10^{-1}
0.4
0.6
0.8
1
1.2
1.4
1.6
1.8

figure 3.png

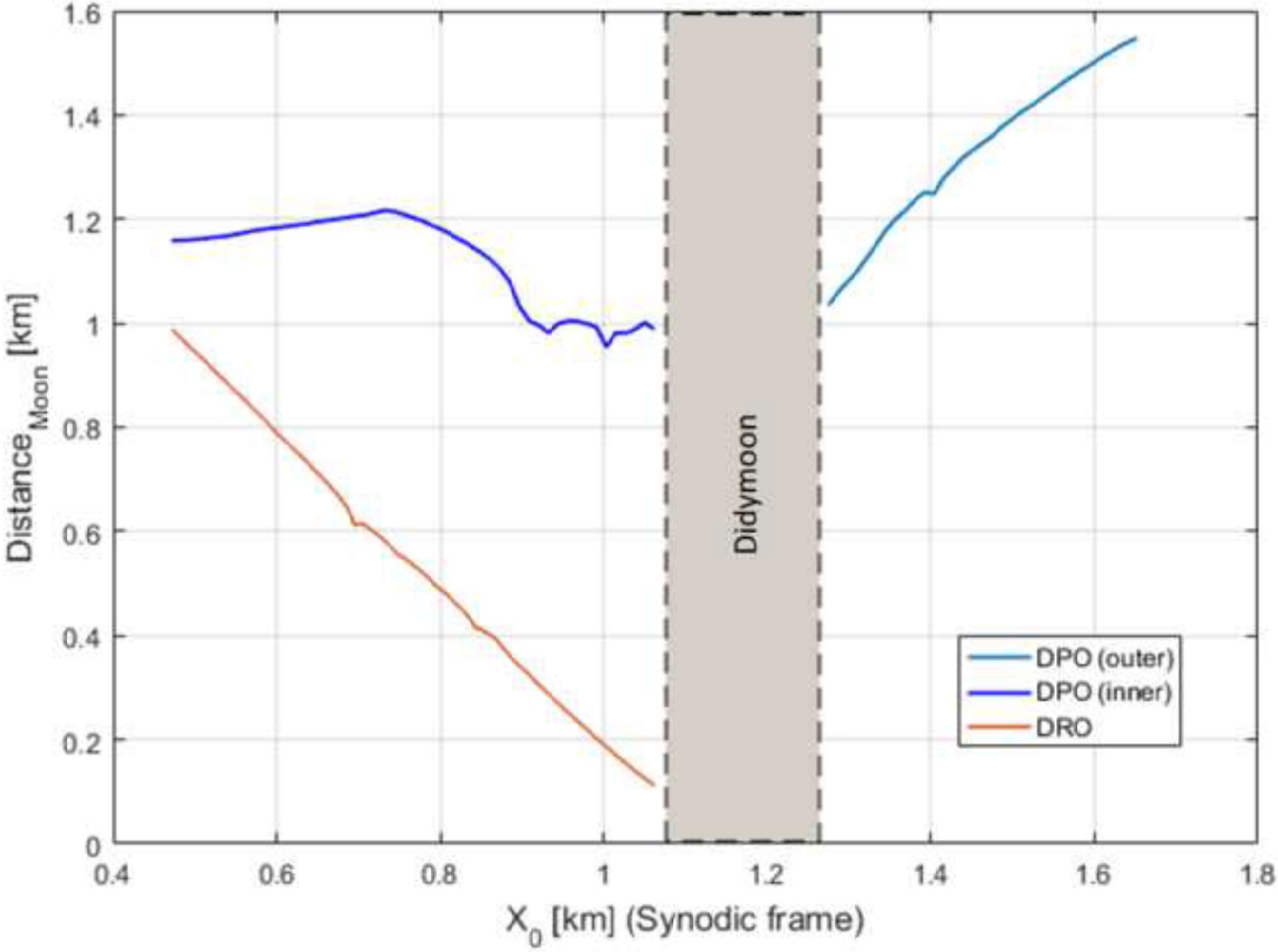
1.6
1.4
1.2
1
0.8
0.6
0.4
0.2
0
0.4
0.6
0.8
1
1.2
1.4
1.6
1.8
Distance Moon [km]
X0 [km] (Synodic frame)
Didymoon
DPO (outer)
DPO (inner)
DRO

figure_4.png

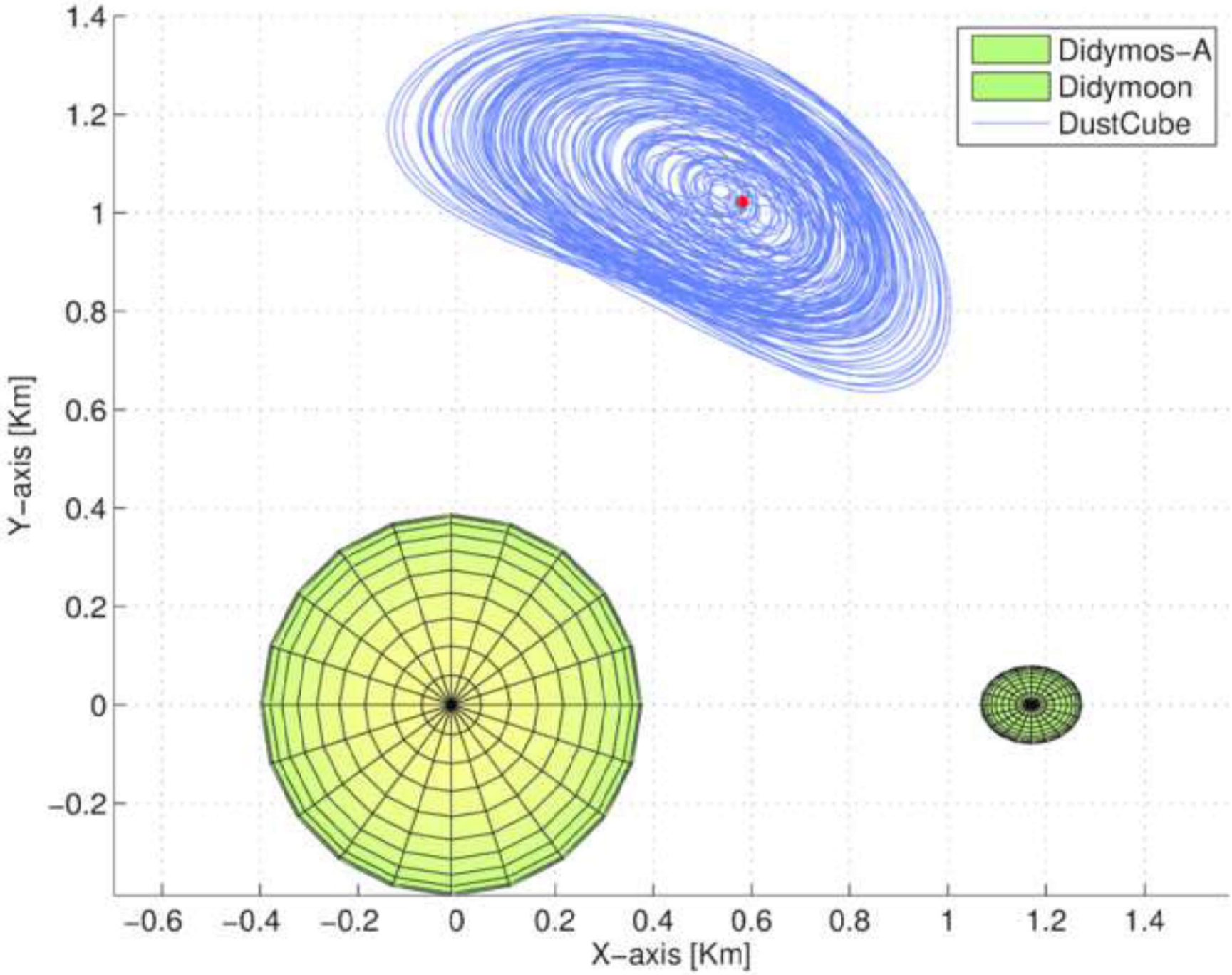
Didymos-A
Didymoon
DustCube
Y-axis [Km]
X-axis [Km]
1.4
1.2
1
0.8
0.6
0.4
0.2
0
-0.2
-0.6
-0.4
-0.2
0
0.2
0.4
0.6
0.8
1
1.2
1.4

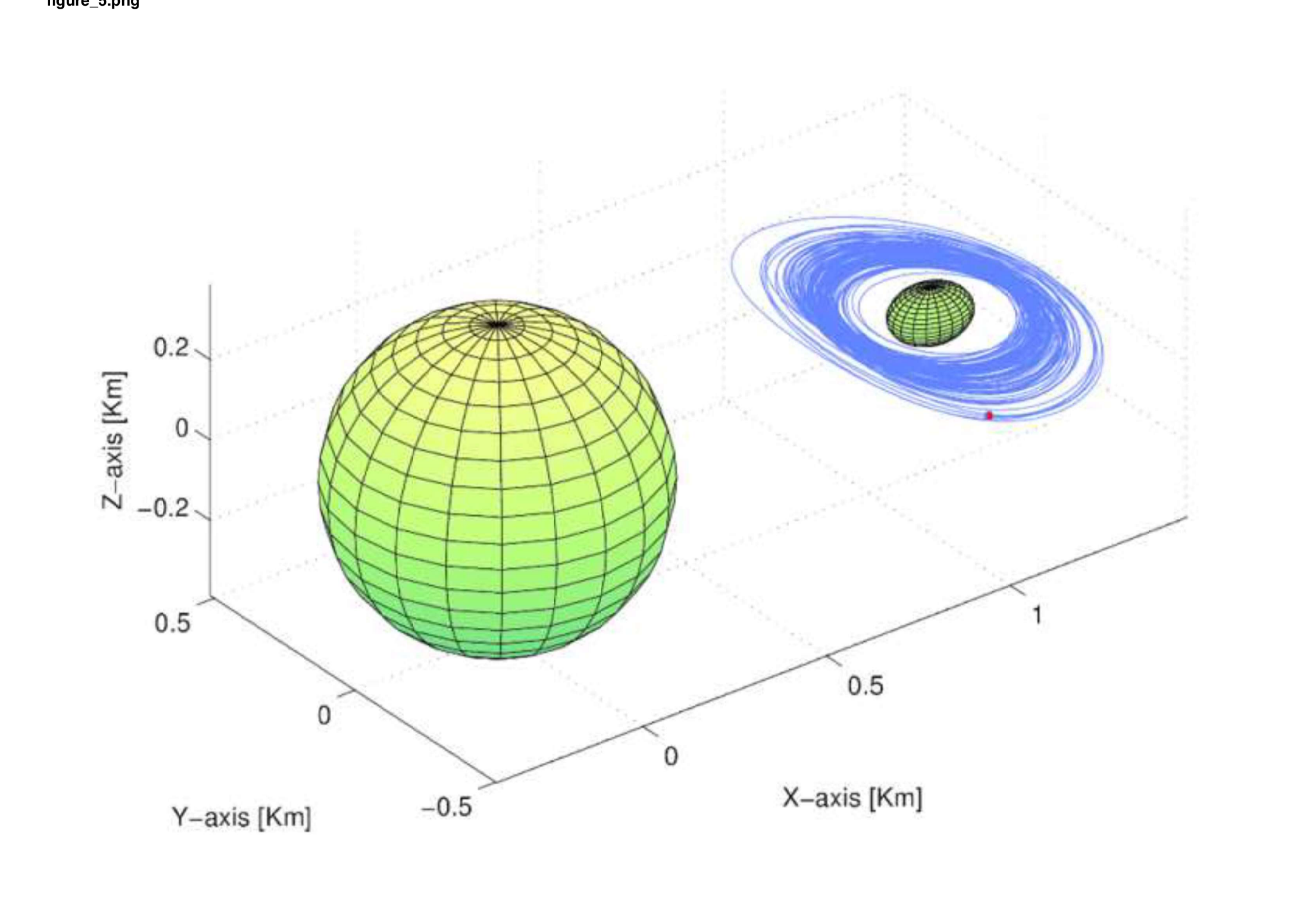
Z−axis [Km]
0.2
0
−0.2
0.5
0
−0.5
Y−axis [Km]
0
0.5
1
X−axis [Km]

figure_6_left.png

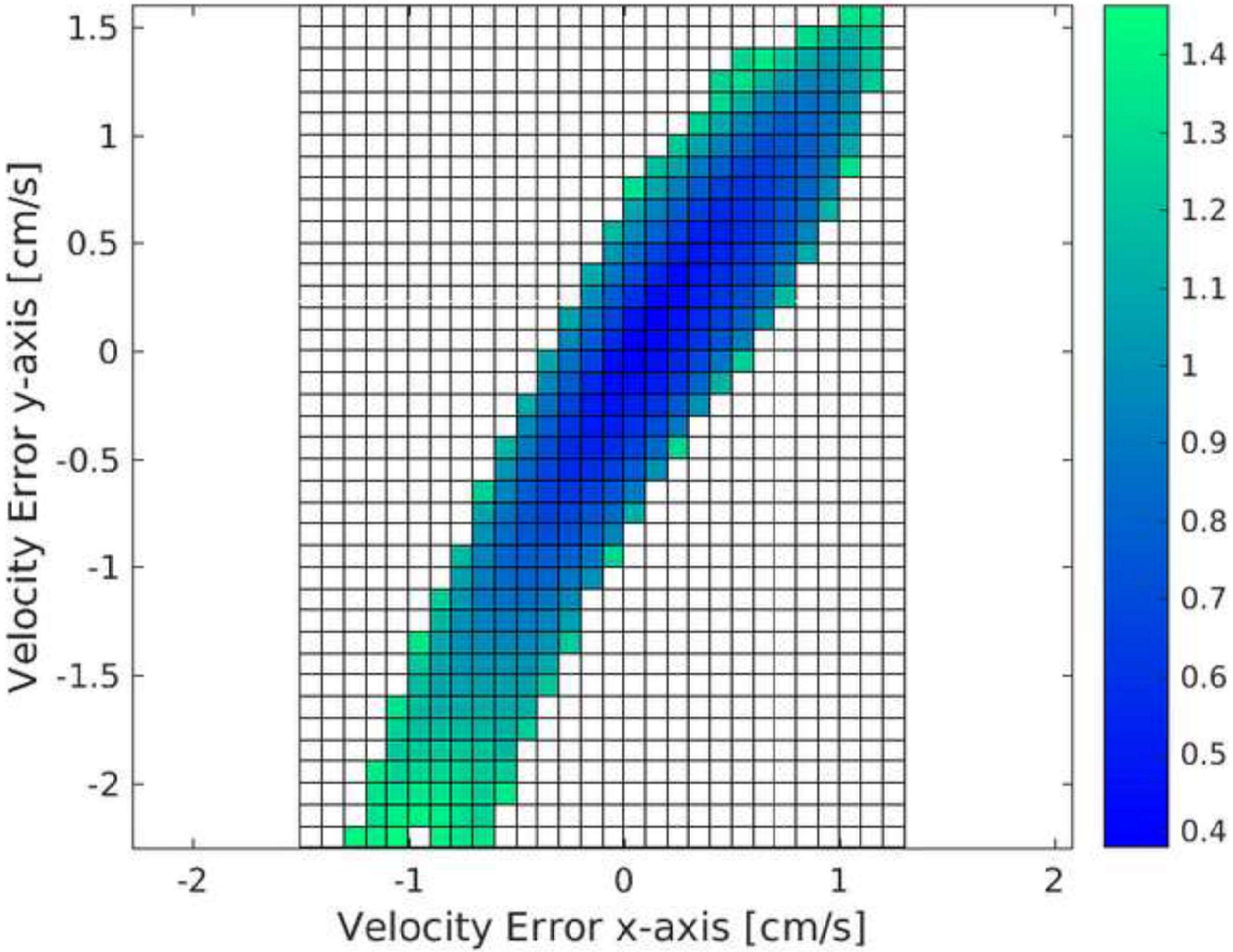

figure_6_right.png

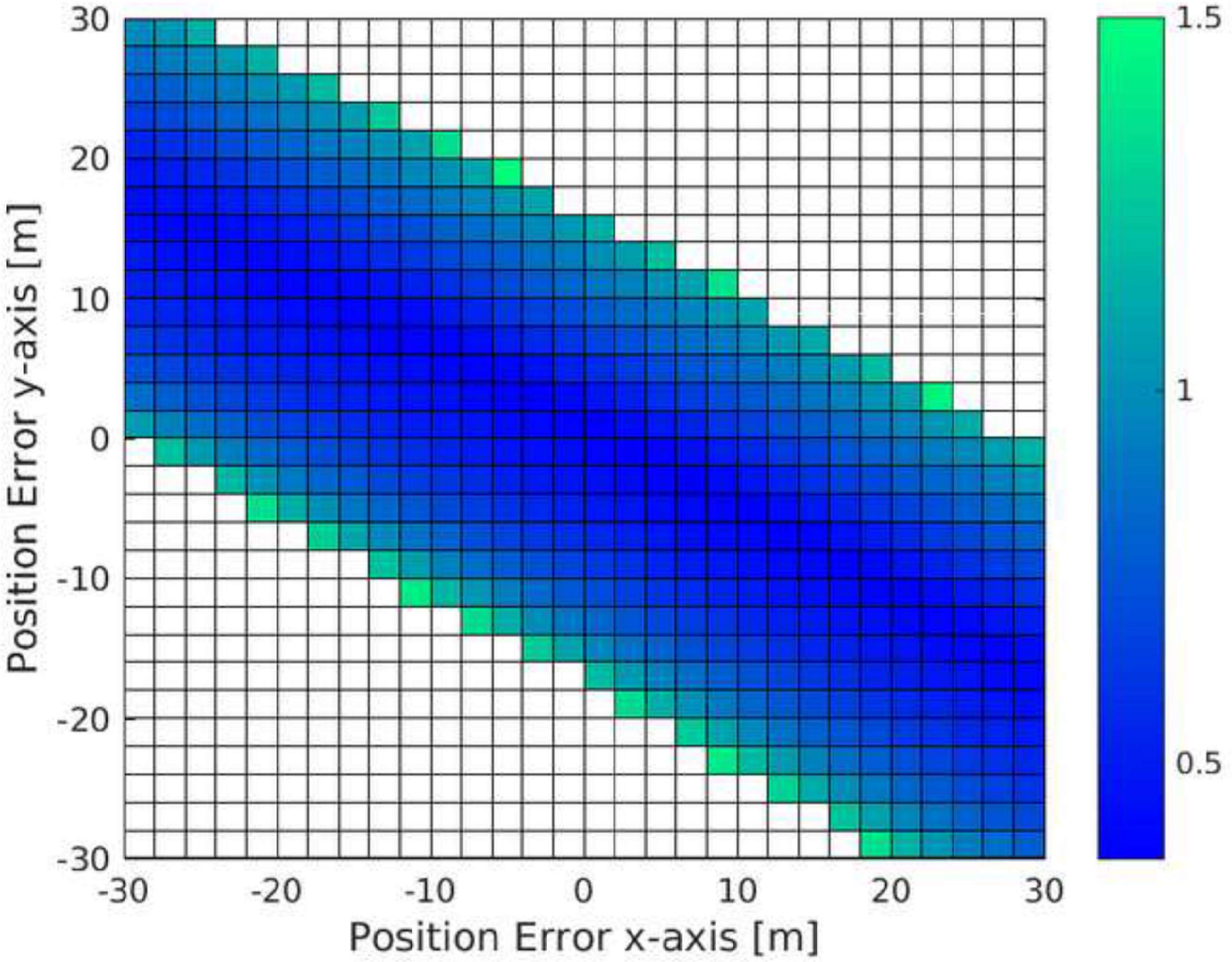

figure_7.png

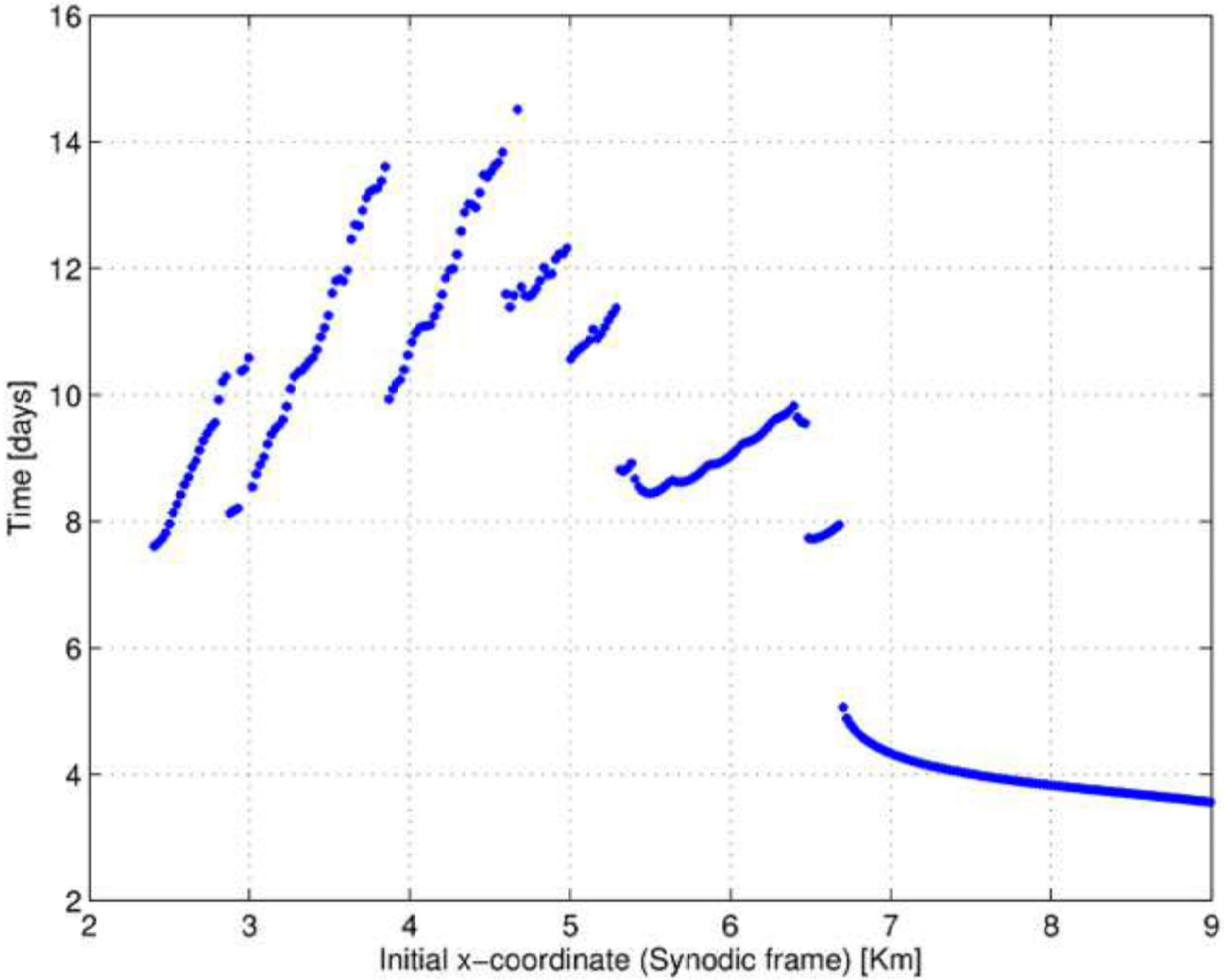
16
14
12
10
8
6
4
2
Time [days]
2
3
4
5
6
7
8
9
Initial x−coordinate (Synodic frame) [Km]

figure_8_left.png

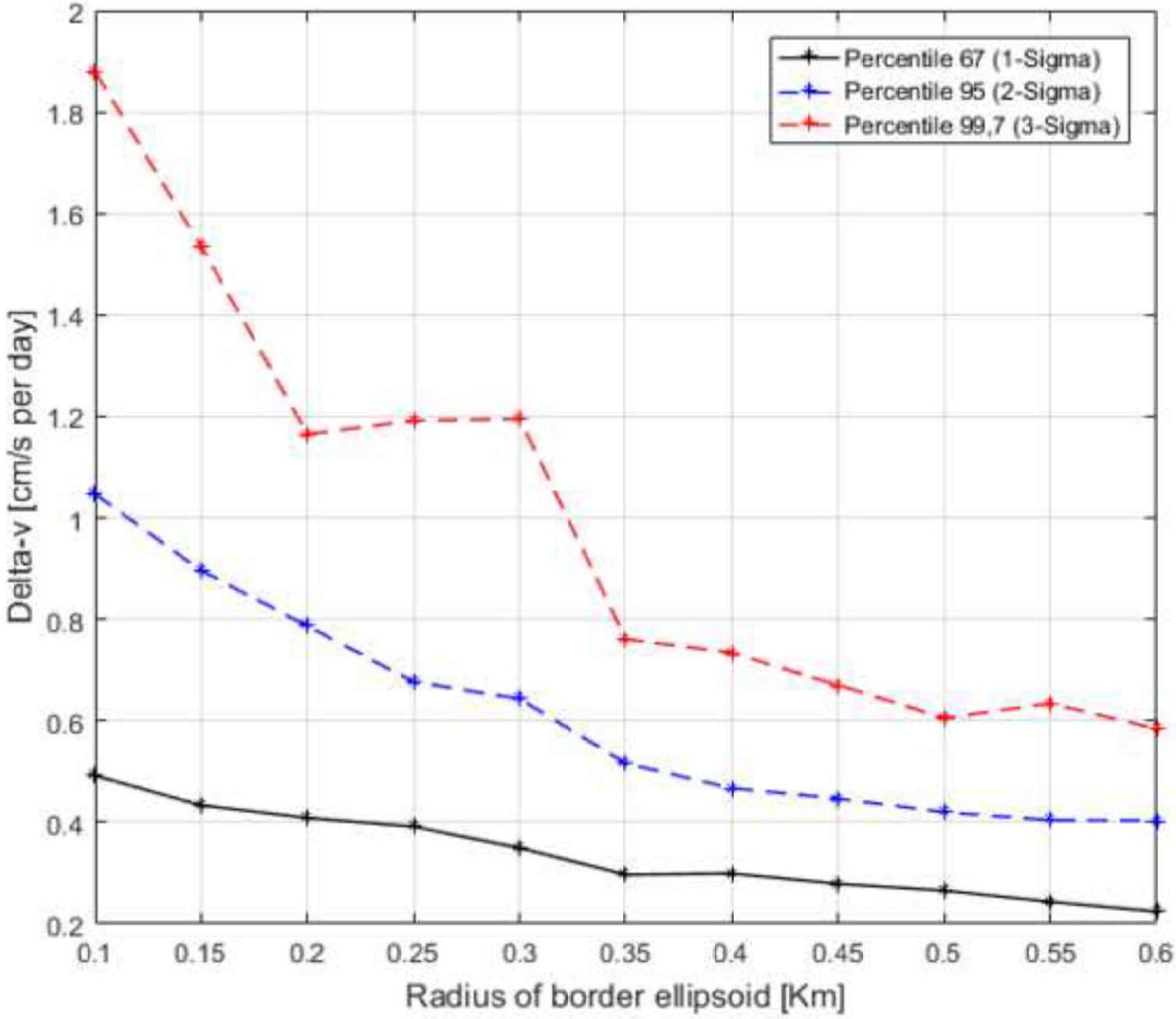

figure_8_right.png

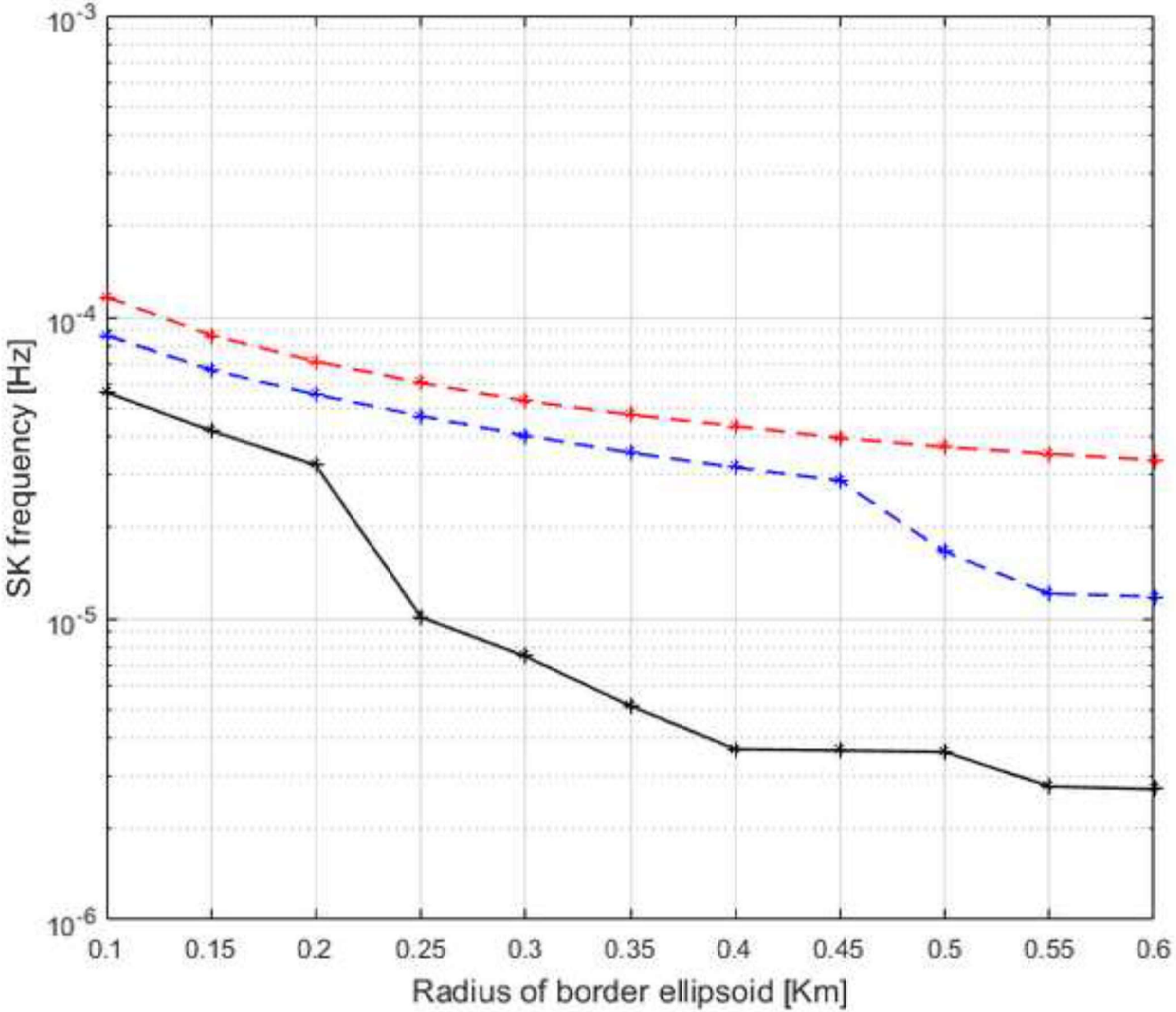

figure_9.png

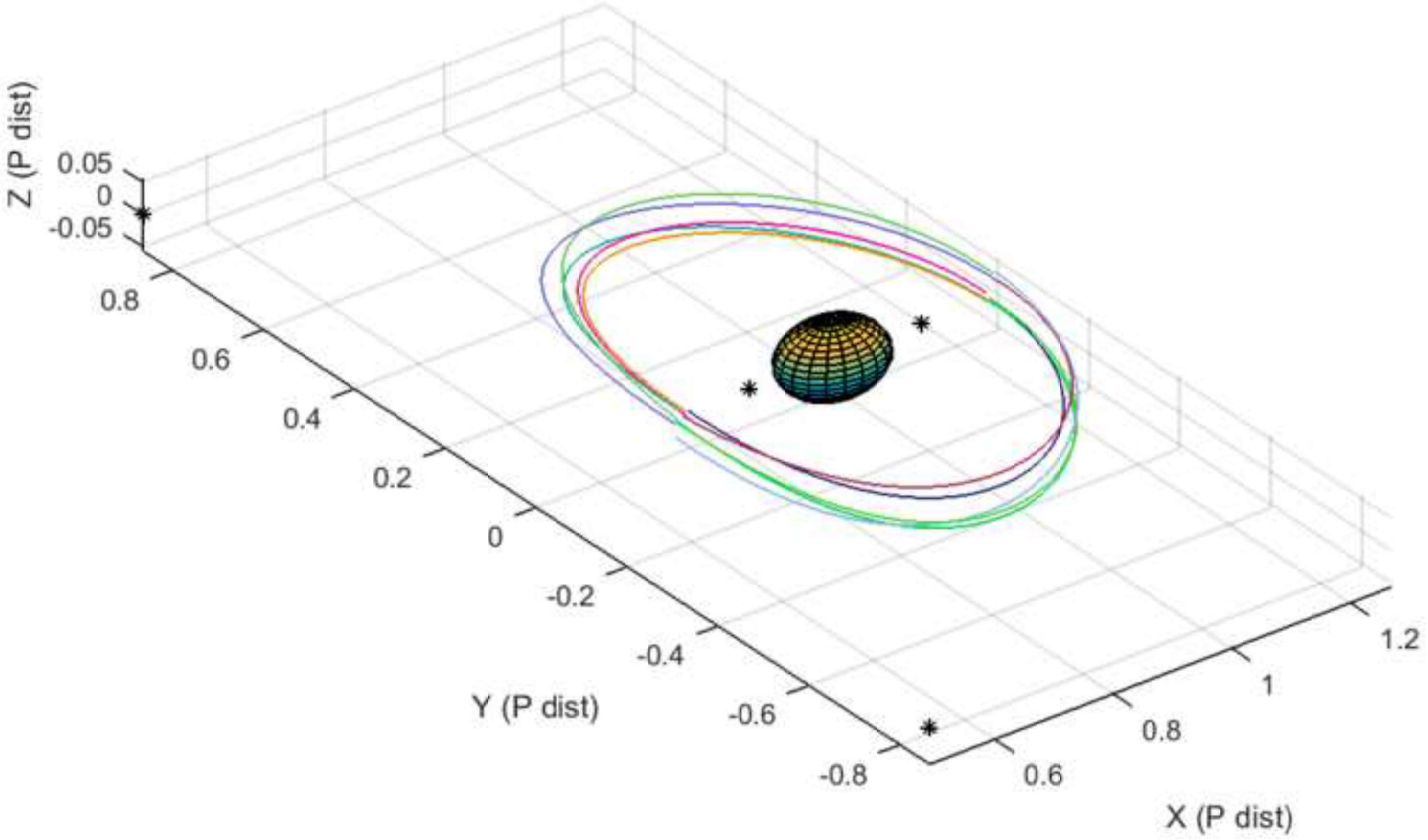

figure_10.png

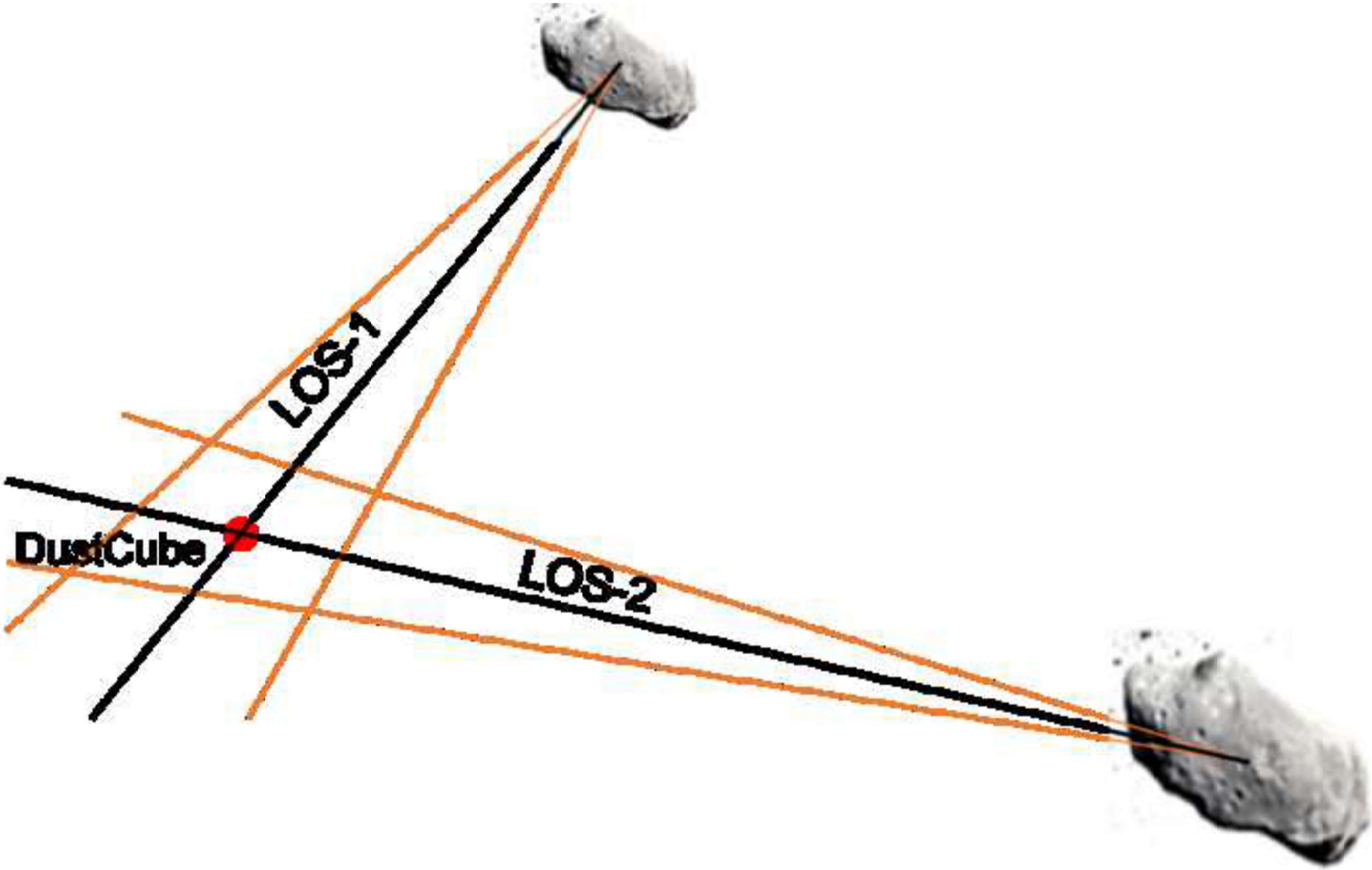

figure_11.png

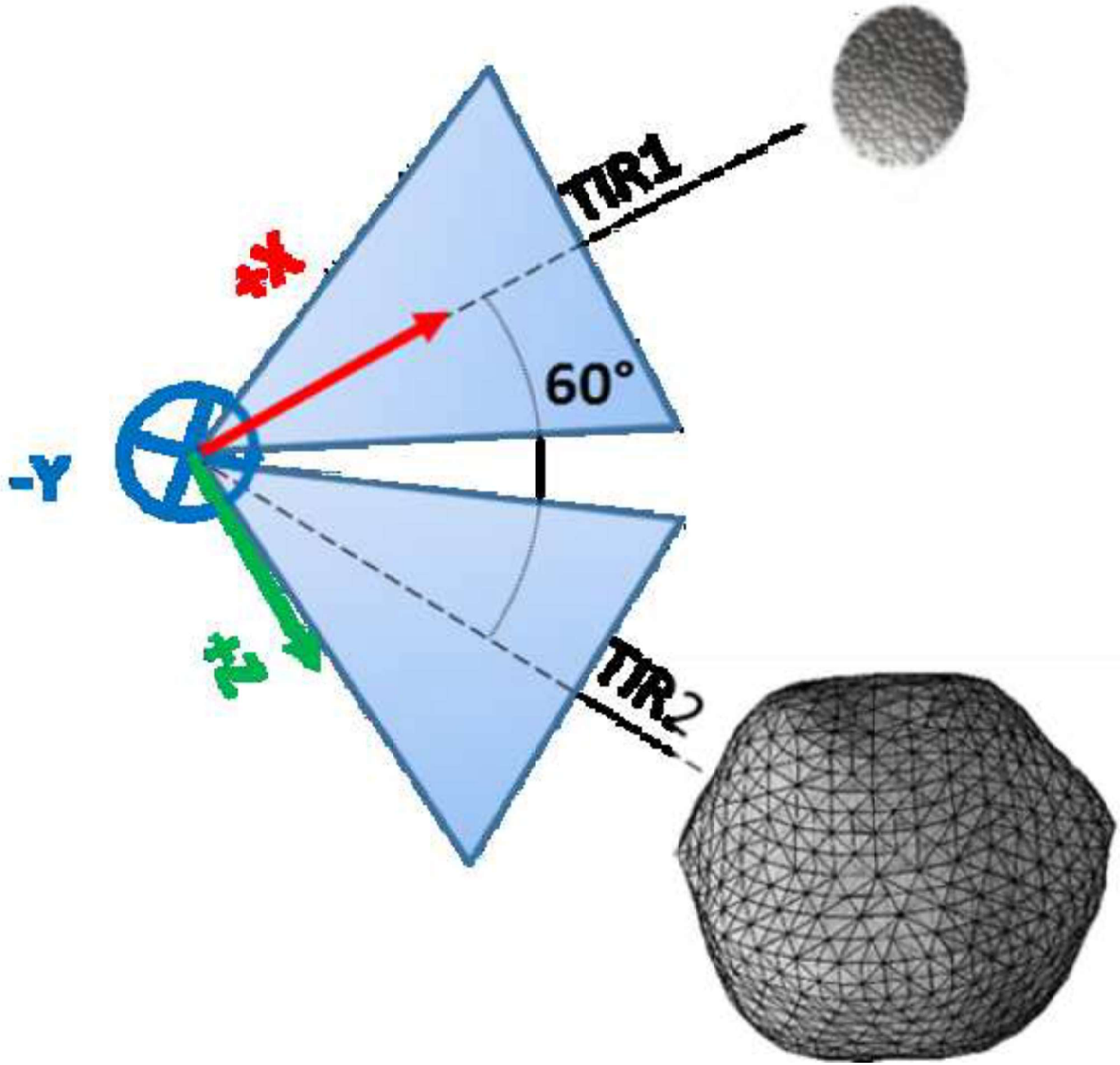

figure_12_left.png

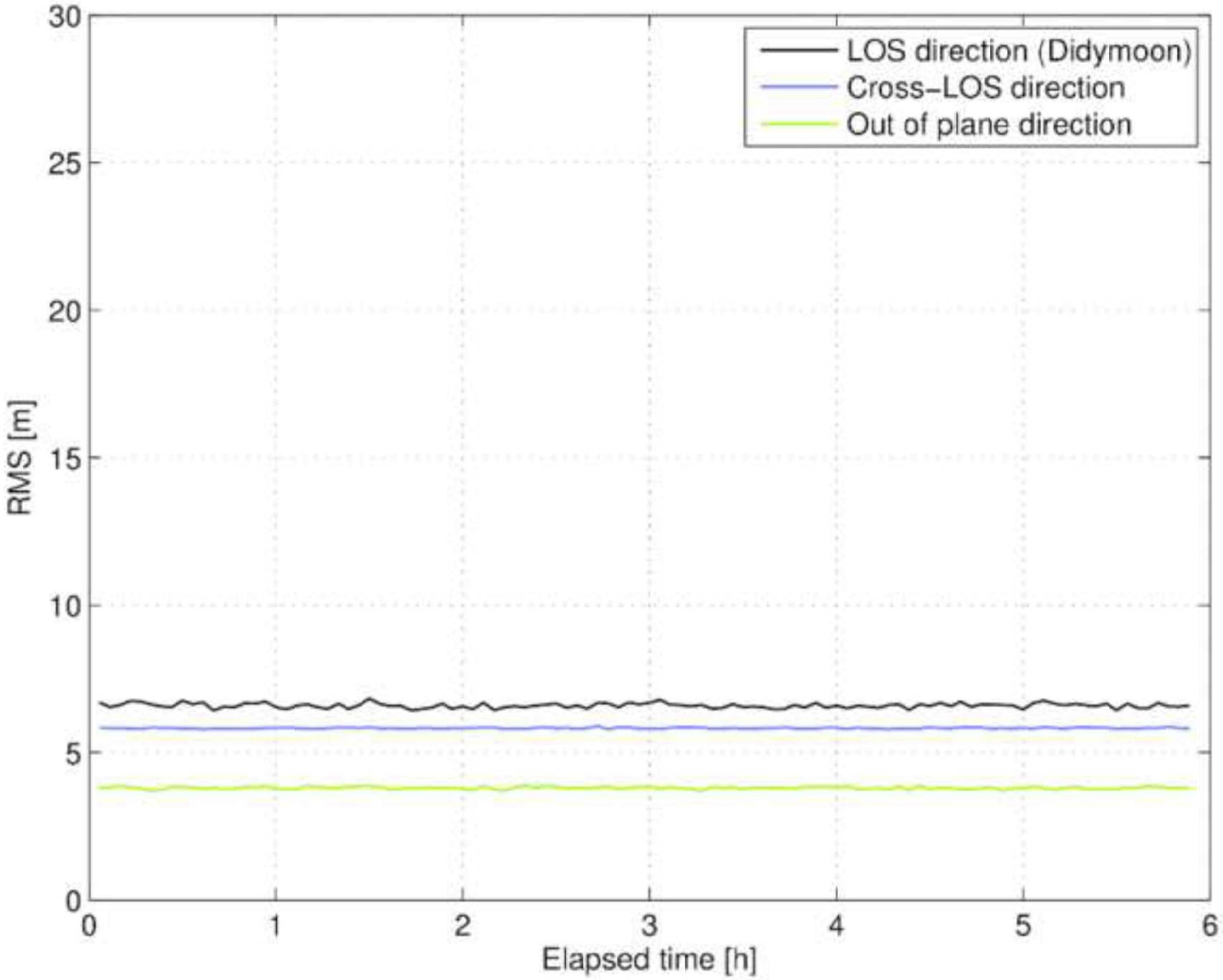

figure_12_right.png

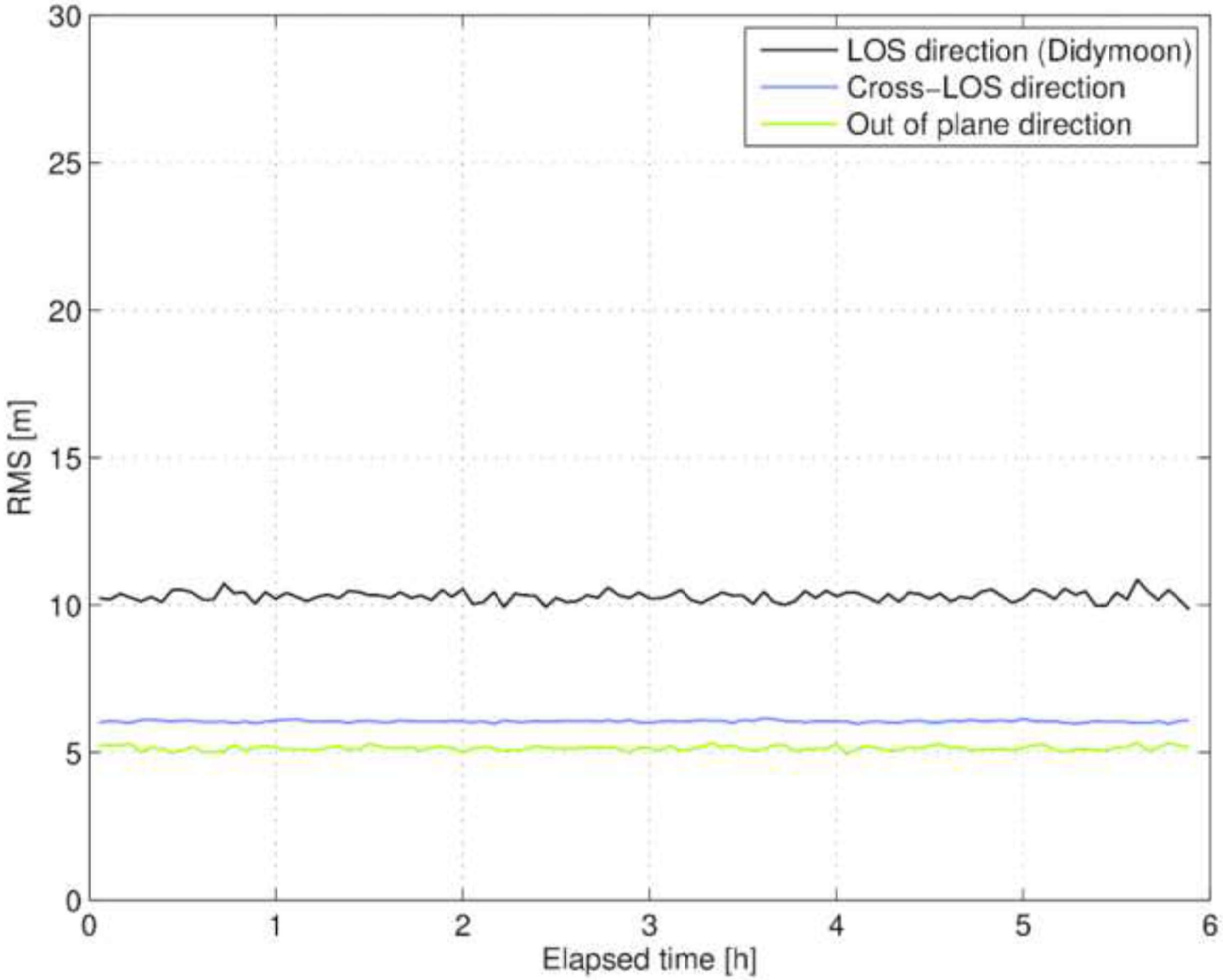

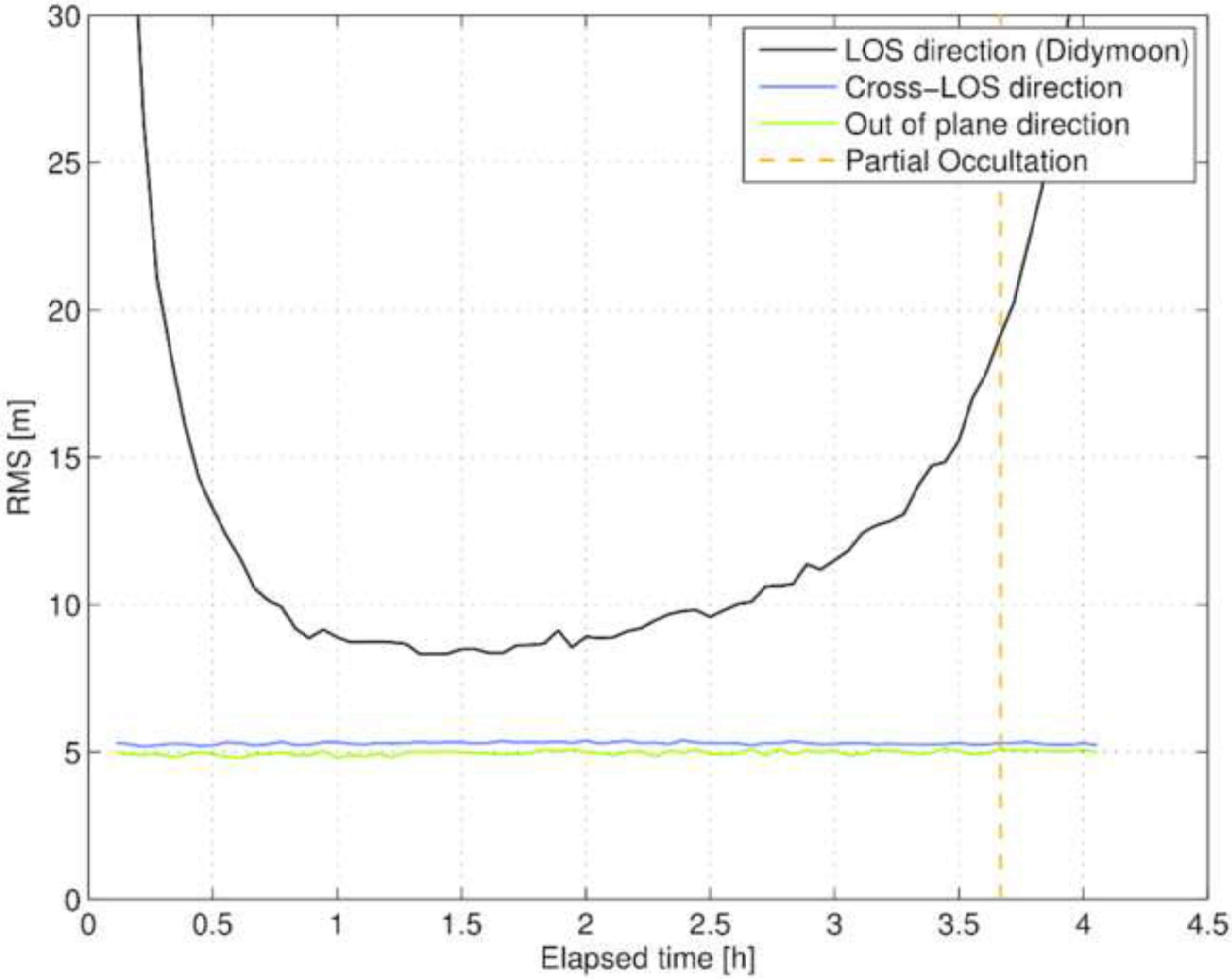
LOS direction (Didymoon)
Cross–LOS direction
Out of plane direction
Partial Occultation
RMS [m]
Elapsed time [h]
0
5
10
15
20
25
30
0
0.5
1
1.5
2
2.5
3
3.5
4
4.5

figure_14.png